An Investigation of the Goshen County, Wyoming, Tornadic Supercell of 5 June 2009 Using EnKF Assimilation of Mobile Mesonet and Radar Observations Collected during VORTEX2. Part II: Mesocyclone-Scale Processes Affecting Tornado Formation, Maintenance, and Decay

JAMES MARQUIS,[a] YVETTE RICHARDSON, AND PAUL MARKOWSKI

Department of Meteorology, The Pennsylvania State University, University Park, Pennsylvania

JOSHUA WURMAN, KAREN KOSIBA, AND PAUL ROBINSON

Center for Severe Weather Research, Boulder, Colorado

(Manuscript received 27 November 2015, in final form 4 June 2016)

ABSTRACT

Storm-scale and mesocyclone-scale processes occurring contemporaneously with a tornado in the Goshen County, Wyoming, supercell observed on 5 June 2009 during the second Verification of the Origins of Rotation in Tornadoes Experiment (VORTEX2) are examined using ensemble analyses produced by assimilating mobile radar and in situ observations into a high-resolution convection-resolving model. This paper focuses on understanding the evolution of the vertical structure of the storm, the outflow buoyancy, and processes affecting the vertical vorticity and circulation within the mesocyclone that correspond to changes in observed tornado intensity.

Tornadogenesis occurs when the low-level mesocyclone is least negatively buoyant relative to the environment, possesses its largest circulation, and is collocated with the largest azimuthally averaged convergence during the analysis period. The average buoyancy, circulation, and convergence within the near-surface mesocyclone (on spatial scales resolved by the model) all decrease as the tornado intensifies and matures. The tornado and its parent low-level mesocyclone both dissipate surrounded by a weakening rear-flank downdraft. The decreasing buoyancy of parcels within the low-level mesocyclone may partly be responsible for the weakening of the updraft surrounding the tornado and decoupling of the mid- and low-level circulation. Although the supply of horizontal vorticity generated in the forward flank of the storm increases throughout the life cycle of the tornado, it is presumably less easily tilted and stretched on the mesocyclone-scale during tornado maturity owing to the disruption of the low-level updraft/downdraft structure. Changes in radar-measured tornado intensity lag those of ensemble Kalman filter (EnKF) mesocyclone vorticity and circulation.

1. Introduction

Using high-resolution mobile radar, in situ, and photogrammetric observations collected during the second Verification of the Origins of Rotation in Tornadoes Experiment (VORTEX2; Wurman et al. 2012), recent studies have investigated the finescale processes leading to tornadogenesis and maintenance in the Goshen County, Wyoming, tornadic supercell that occurred on 5 June 2009. Wakimoto et al. (2011, 2012) and Atkins et al. (2012) documented the width and vertical structure of the tornado-bearing vortex and vertical motions within it using single- and dual-Doppler winds. Among other findings, they concluded that angular momentum within the mesocyclone was not well correlated with tornado intensity. Markowski et al. (2012a,b) described the origins of the low-level mesocyclone and showed how a descending precipitation core and rear-flank outflow abruptly increased the low-level angular momentum just prior to tornadogenesis. Kosiba et al. (2013) concluded that a rear-flank downdraft (RFD) surge likely played a role in the intensification of the near-surface vortex to tornado strength. Richardson

[a] Current affiliation: Center for Severe Weather Research, Boulder, Colorado.

Corresponding author address: James N. Marquis, Center for Severe Weather Research, 1945 Vassar Cir., Boulder, CO 80305.
E-mail: jmarquis@cswr.org

DOI: 10.1175/MWR-D-15-0411.1

et al. (2012) related oscillations in the intensity of the tornado to bands of radar reflectivity and discrete patches of vertical vorticity spiraling around it during its mature phase and speculated that an area of precipitation falling along the vertical axis of rotation was associated with enhanced downdraft within the tornado that caused it to dissipate. French et al. (2014) surmised that strong vertical shear of the tornado-relative horizontal winds over its depth made the vortex increasingly tilted and hypothesized that the development of the tilt was linked to the weakening of the tornado aloft prior to near the surface.

The aforementioned studies have exposed some of the finescale processes that may affect tornado formation, maintenance, and decay. However, gaps unavoidably are present in observational data owing to a limited number of radars, surface-based probes being confined to drivable roads, and the paucity of in situ observations collected aloft within any storm. These deficiencies preclude a more complete understanding of the processes that might affect the formation, maintenance, and dissipation of the tornado.

Marquis et al. (2014a, hereafter Part I) assimilated the mobile radar velocity and mobile mesonet thermodynamic observations collected in the Goshen storm into a cloud-resolving numerical model using the ensemble Kalman filter (EnKF) technique. Many details of the EnKF analyses agreed well with dual-Doppler observations and parcel trajectories calculated from them. Furthermore, assimilating mobile mesonet thermodynamic observations decreased the sensitivity of cold pool temperature to model microphysics parameterizations, increasing confidence in the estimates of outflow buoyancy. Therefore, we expect the ensemble analyses produced in Part I to be a valuable tool for evaluating storm dynamics and influences on the tornado life cycle that cannot be determined with observations alone.

The purpose of this paper is to relate the life cycle and finescale properties of the Goshen County tornado documented in past studies to mesocyclone-scale and storm-scale[1] properties of the parent supercell resolved in our model ensemble (analysis grid spacing and time step: $\Delta x = 500$ m, $\Delta t = 2$ min). To accomplish this goal, we relate unsmoothed single-Doppler velocity observations of tornado intensity to processes represented in the EnKF ensemble-mean kinematic and thermodynamic analyses described in Part I. Particular storm processes of interest include changes in the low-level and midlevel[2] updraft, an RFD surge, mesocyclone-scale circulation, outflow buoyancy, and horizontal vorticity generated along parcel trajectories passing through the mesocyclone. These and other aspects of the storm-scale flow also are discussed in the context of the finer-scale features described in previous studies to better understand their possible roles in tornado formation, maintenance, and decay.

2. Tornado life cycle

The Goshen County tornado, whose life cycle was documented by the Doppler on Wheels (DOW) in Kosiba et al. (2013; illustrated in Fig. 1), lasted approximately 25–30 min, reached a peak intensity[3] of $\Delta V \approx 115\ \mathrm{m\ s^{-1}}$, contained a wind speed of $58\ \mathrm{m\ s^{-1}}$ measured at $z = 3$ m AGL (Wurman et al. 2013), and was rated an EF2 on the enhanced Fujita (EF) scale. In this article, we define the *tornadogenesis period* to be from 2153 to 2202 UTC. The exact time of tornadogenesis is ambiguous in this case owing to fluctuations in ΔV above and below $40\ \mathrm{m\ s^{-1}}$ during this time period ($40\ \mathrm{m\ s^{-1}}$ has been used in past mobile radar studies to identify vortices as tornadoes; e.g., Alexander and Wurman 2008). The tornado strengthened between approximately 2202 and 2212 UTC (here called the *intensification period*), after which it remained comparatively steady in intensity from approximately 2212 to 2218 UTC (the *maturity period*). Observations from the MWR-05XP mobile phased array radar (French et al. 2014) suggest that the strongest vorticity associated with the Goshen tornado was in the lowest 200 m and between 2217 and 2219 UTC, qualitatively agreeing with DOW6 and DOW7 observations. The *weakening period* began at 2218 UTC.[4] By 2226 UTC, ΔV dropped below $40\ \mathrm{m\ s^{-1}}$, and all traces of the tornado are gone by 2230 UTC. These observations of the tornado life cycle are discussed in the context of the EnKF storm-scale analyses below.

[1] We use "tornado scale," "mesocyclone scale," and "storm scale" to characterize, respectively, processes occurring on the following spatial scales: less than 1 km, between 1 and 4 km, and greater than 4 km.

[2] Low-level and midlevel features are prescribed to span heights of $0 \le z \le 2.5$ km, and $2.5 \le z \le 7$ km, respectively. These ranges are arbitrarily divided at 2.5 km because this is the approximate LFC in the base-state environment, and it is just above the depth of the outflow air (further discussed in section 4).

[3] Defined as the difference between peak inbound and outbound extrema of a radar radial velocity couplet ΔV at the lowest beam elevation angle.

[4] There is some disagreement between DOWs about the exact time when the tornado began to weaken, depending on their distance to the tornado (thus, spatial resolution of observations). The closest (rapid scan) DOW observed an oscillation in peak ΔV during the defined weakening period before the tornado quickly decayed at 2225 UTC.

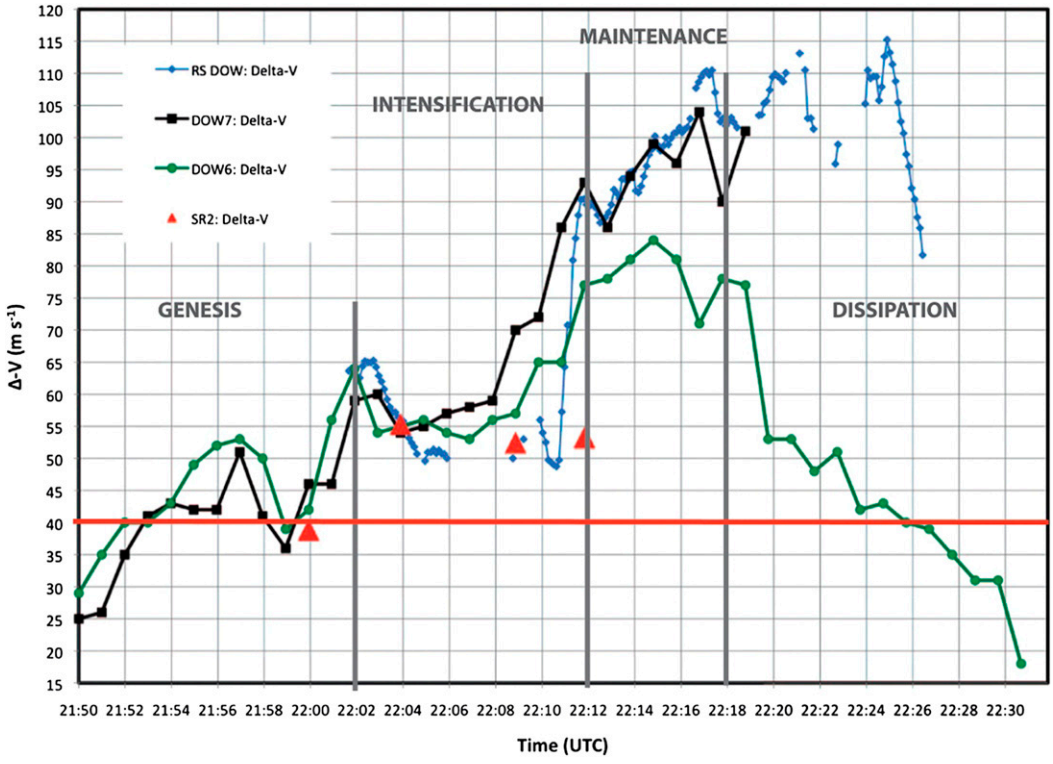

FIG. 1. Difference between peak unsmoothed inbound and outbound single-Doppler radial velocity, ΔV, from the rapid scan DOW, DOW7, DOW6, and Shared Mobile Atmospheric Research and Teaching Radar (SMART-R2) radars throughout the life cycle of the tornado. Tornadogenesis, intensification, maturity (maintenance), and dissipation stages are labeled. Measurements are made using the 1.0° beam elevation angle; beam heights at the tornado vary by radar and generally are $z \sim 300$ m and ≤ 50 m during tornadogenesis and demise, respectively. Measurements of ΔV may be underestimated more during the tornadogenesis period than later in the tornado life cycle, owing to the generally greater distance between the radars and the tornado early in the deployment. From Kosiba et al. (2013).

3. General storm structure and evolution

The evolution of the low-level storm structure surrounding the tornado depicted by EnKF ensemble-mean analyses (all analyses herein are ensemble-mean fields valid immediately after assimilation) is shown in Fig. 2. A relatively weak pretornadic mesocyclone is located just west of where the rear-flank gust front and the forward-flank boundary[5] intersect (Fig. 2a). There are no obvious additional narrow convergence or thermodynamic boundaries located within the forward-flank region of the storm (e.g., Beck and Weiss 2013; Weiss et al. 2015). The strongest downdraft at low levels on the rear flank of the storm is located ~2–5 km horizontal distance from the mesocyclone and is more broadly distributed and weaker relative to future times. During the period of tornadogenesis (Figs. 2b,c), vertical vorticity within the mesocyclone increases substantially, the RFD wraps around the circulation center, and a band of ascent develops southwest of the vorticity maximum, downstream from a local maximum in RFD intensity. This band of updraft resembles the "secondary gust fronts" or "internal momentum surge boundaries" found in other supercells (e.g., Wurman et al. 2007; Finley and Lee 2008; Lee et al. 2008; Wurman et al. 2010; Lee et al. 2012; Marquis et al. 2012; Kosiba et al. 2013; Skinner et al. 2014). A distinct downdraft maximum (possibly an occlusion downdraft; Klemp and Rotunno 1983) forms just south-southeast of the vorticity maximum.

The RFD surge and cold outflow from the forward flank wraps cyclonically around the mesocyclone between the time of tornado formation and maturity (Figs. 2b–e). As a result, the tornado becomes increasingly displaced from the ambient environmental

[5] We refer to this as a "boundary" rather than a "gust front," as in many past studies, because of the weak convergence and relative diffuseness of the wind shift across it.

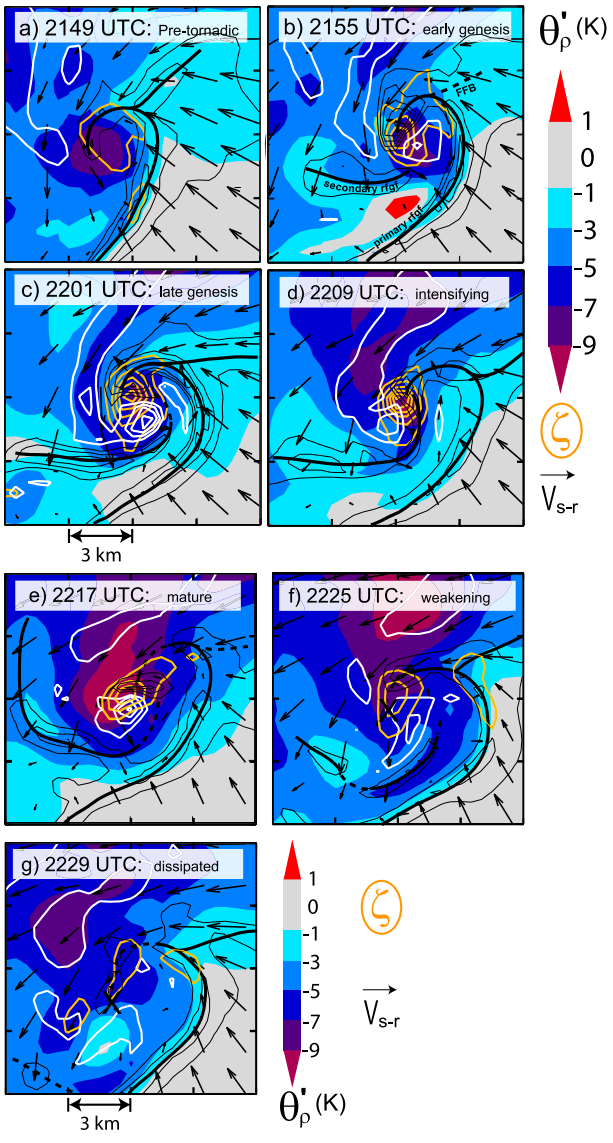

FIG. 2. (a)–(g) Ensemble-mean density potential temperature perturbation from the environment (shaded), storm-relative horizontal wind (vectors; only every fourth vector shown for clarity), updraft (thin black contours; outermost contour is 0.25 m s^{-1} incremented by 0.25 m s^{-1}), downdraft (white contours; outermost contour is −0.75 m s^{-1}, incremented by −0.75 m s^{-1}), and positive vertical vorticity (orange contours; outermost contour is 0.01 s^{-1}, incremented by 0.01 s^{-1}) at z = 200 m at seven times throughout the life cycle of the tornado. Vertical velocity maxima along the near-surface gust fronts are traced with bold black lines. An "×" in (f) and (g) marks the location of the dissipating tornado.

air. As the tornado matures, the RFD weakens west of the mesocyclone but remains strong immediately south of it (Fig. 2e). The established low-level updraft–downdraft structure surrounding the mesocyclone and tornado disintegrates as the tornado transitions to its weakening phase (Figs. 2e–g). The strong isolated downdraft just south of the mesocyclone weakens and broadens, and the secondary gust front leading it has progressed eastward relative to earlier times such that it merges with the primary rear-flank gust front. This evolution of the low-level outflow and attendant rear-flank gust front (a portion of which is occluded with the forward-flank boundary) wrapping around the mesocyclone and the mixture of updraft and downdraft within the mesocyclone gradually becoming mostly downdraft throughout the tornado life cycle (schematically summarized in Fig. 3) is qualitatively consistent with typical past descriptions of supercell evolution (e.g., Lemon and Doswell 1979; Klemp and Rotunno 1983; Wicker and Wilhelmson 1995), but with the storm also containing an RFD surge, as seen in several recent studies (e.g., Marquis et al. 2008; Wurman et al. 2010; Marquis et al. 2012; Skinner et al. 2014 Schenkman et al. 2014). Storm-relative flow in the forward flank of the storm is mainly easterly or east-southeasterly, as in the environment (e.g., Frame et al. 2009; Beck and Weiss 2013). The strongest low-level downdraft generally is found in an area extending from the rear-flank region northeastward into the forward flank rather than as isolated rear-flank and forward-flank downdrafts.

During the pretornadic phase, the largest peak vertical vorticity in the storm is located at midlevels (e.g., z = 3–4 km; Fig. 4a). Preceding an abrupt increase in near-surface (e.g., $z \leq 200$ m) rotation during the tornadogenesis phase (~2155 UTC), vertical vorticity strengthens at progressively lower heights below 3 km between 2150 and 2155 UTC. Enhanced stretching of vertical vorticity accompanies this trend (Fig. 4b). It is possible that this is related to changes in angular momentum fluxes associated with a descending reflectivity core that is occurring around this time (Markowski et al. 2012a,b); however, such a reflectivity feature is not clearly discernible in the ensemble-mean precipitation fields (see Part I).

After the tornadogenesis stage, the strongest positive stretching occurs near the surface and remains that way through tornado maturity. Vertical vorticity within the mesocyclone nearly simultaneously increases at all heights below 7 km near the end of the tornadogenesis period, and the strongest near-surface vorticity occurs during the transition between tornado intensification and maturity. Peak vorticity within the mesocyclone abruptly weakens at all heights during the period of tornado maturity. Evolution of peak ensemble mean vertical vorticity is qualitatively similar to time–height analyses of peak vorticity using dual-Doppler mobile radar data that are objectively analyzed to a Cartesian grid similar to our model grid spacing (Fig. 5). Although the time–height analysis of dual-Doppler peak vorticity is smoother than in the EnKF analyses, and the strongest dual-Doppler vorticity is generally closer to the ground

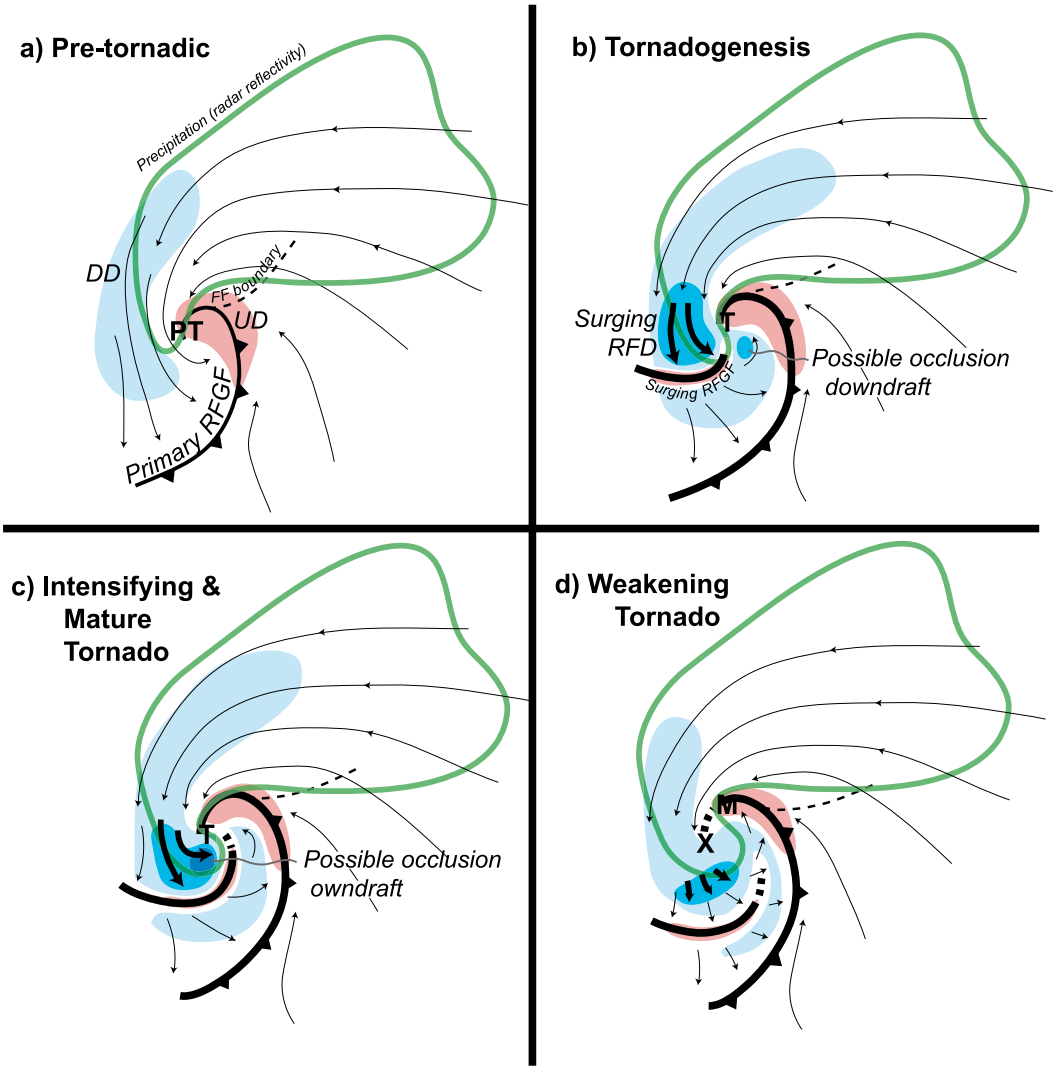

FIG. 3. Schematic diagram of the low-level structure of the Goshen supercell during the life of the tornado, including areas of downdraft (DD; blue), the rear- and forward-flank outflow boundaries, the main updraft core (UD; red), horizontal flow (streamlines), and the precipitation core (green outline). PT and T refer to the pre-tornadic vortex and tornado, respectively, while the M and X in (d) indicate the location of a newly forming low-level mesocyclone and the dissipating tornado, respectively.

than in EnKF analyses, this comparison suggests an overall realistic strengthening and weakening of mesocyclone-scale vertical vorticity captured by the EnKF analyses between 2150 and 2155 UTC and after 2216 UTC, respectively. Qualitatively similar vorticity features shown in dual-Doppler analyses that resolve finer spatial scales (Atkins et al. 2012; cf. our Fig. 4a, their Fig. 6) (e.g., a downward progression of the most intense vertical vorticity from $z = 2$ km to near the surface) lag those in our EnKF analyses by approximately 8 min. This may suggest that trends in tornado intensity lag those of the mesocyclone.

Although the peak of near-surface vertical vorticity remains underneath the western edge of the midlevel updraft throughout the life cycle of the tornado, the midlevel updraft core travels eastward slightly faster than the near-surface mesocyclone (or is perhaps weakened above the surface mesocyclone owing to a downward-pointing vertical perturbation pressure gradient force associated with it; Fig. 6). The mesocyclone is most vertically erect during the tornado intensification and maturity phases and is most tilted in a southwest–northeast orientation during the weakening phase of the tornado, generally consistent with the vertical structure shown in Richardson et al. (2012) and French et al. (2014). This tilt is likely due to the enhanced low-level northeasterly outflow within the northwestern portion of the dissipating mesocyclone (Figs. 2f,g), consistent

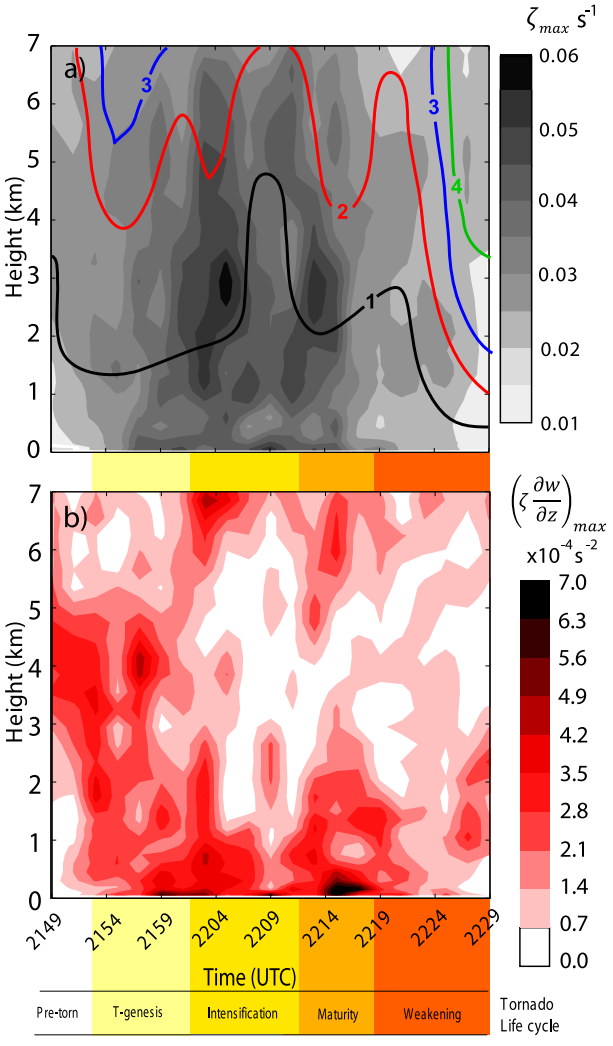

FIG. 4. (a) Peak vertical vorticity within the mesocyclone as a function of height and time throughout the life cycle of the tornado. The horizontal displacement from the near-surface vorticity maximum at each height is contoured (km). (b) Instantaneous stretching of vertical vorticity at the vorticity maximum. Pretornadic, tornadogenesis, intensification, maturity, and weakening periods are highlighted in yellow–orange shading.

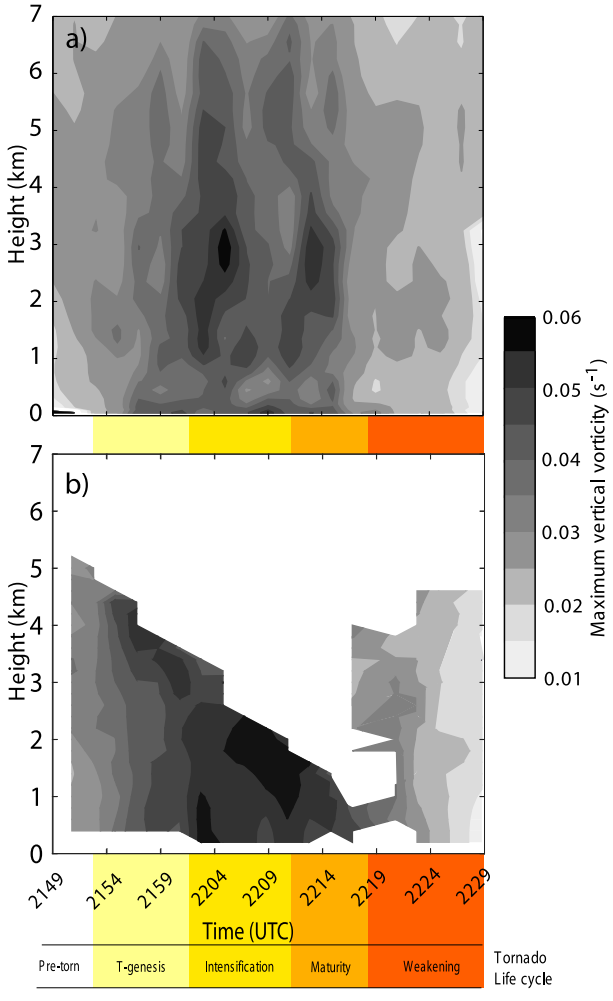

FIG. 5. (a) As in Fig. 4a. (b) As in Fig. 4a, but performed using dual-Doppler wind syntheses between DOW6 and DOW7 (prior to 2216 UTC) and DOW6 and NOXP (after 2216 UTC). Dual-Doppler analyses are produced like those shown in Part I of this study, including objectively analyzed radar data using Cressman smoothing with a cutoff radius of 800 m, a Cartesian grid with 500-m (200 m) horizontal (vertical) grid spacing, and iterative upward integration of mass continuity. White space in (b) is missing data.

with vertically varying horizontal advection of vertical vorticity (e.g., Dowell and Bluestein 2002; Marquis et al. 2012; French et al. 2014). These strong northeasterlies do not appear to be part of the original RFD surge associated with tornadogenesis, which is weaker at the time of tornado dissipation.

4. Relationships between mesocyclone circulation, outflow buoyancy, and the tornado life cycle

Prior research has shown that the buoyancy of the outflow affects the likelihood of tornadogenesis in supercells (e.g., Markowski et al. 2002, 2003; Grzych et al. 2007), but comparatively few studies have assessed the relationship between tornado intensity and outflow temperature evolution after tornadogenesis (Hirth et al. 2008; Lee et al. 2012; Marquis et al. 2012). To investigate this relationship in our analyses, we examine the low-level buoyancy and the circulation ($\Gamma = \oint \mathbf{v} \cdot \mathbf{dl}$) at various heights about horizontal circles (at various radii, as specified in the figure captions) centered on the Goshen mesocyclone (Figs. 7, 8).

Both buoyancy and circulation of the mesocyclone are largest early in the life cycle of the tornado and decrease as it progresses. Atkins et al. (2012) report a similar peak in low-level circulation early in the intensification period

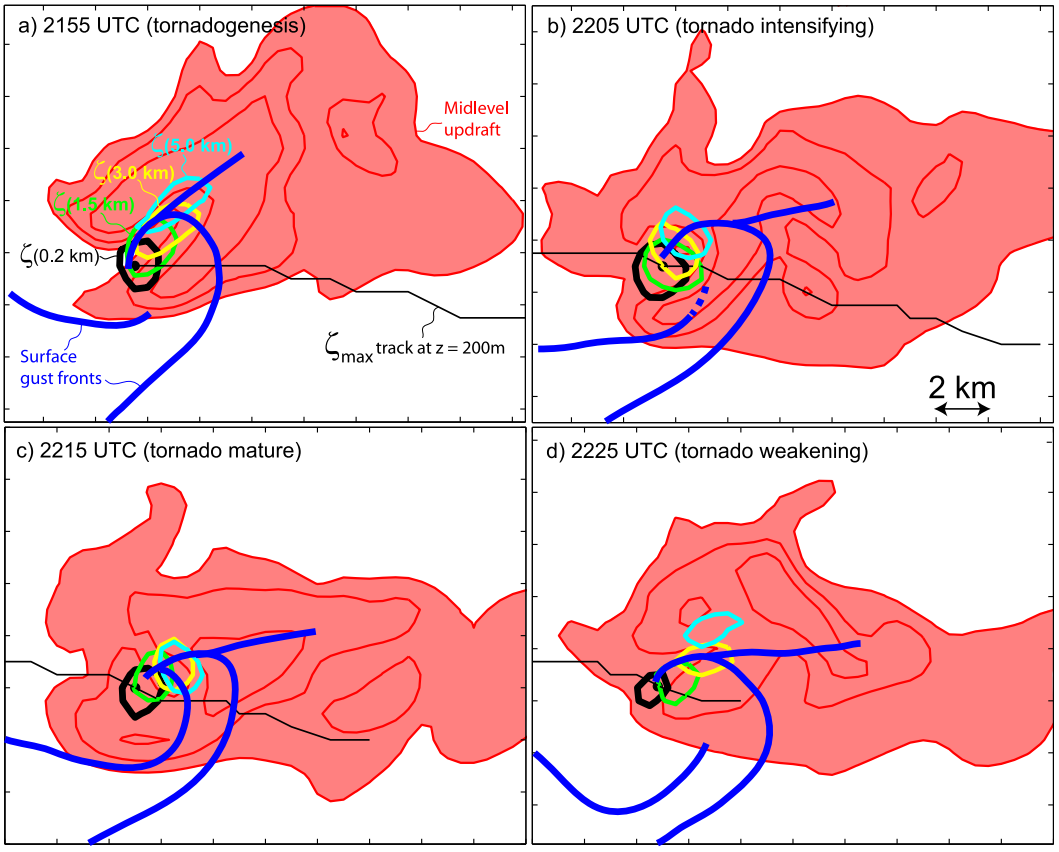

FIG. 6. Ensemble mean $w = 5$, 10, and 15 m s^{-1} at $z = 5$ km (red contours; shading is $w > 5$ m s^{-1}), w maximum along the gust fronts near the ground (traced with thick blue lines), and $\zeta = 0.02$ s^{-1} at $z = 0.2$, 1.5, 3.0, and 5.0 km (thin black, green, yellow, and cyan contours, respectively) at four times throughout the life cycle of the tornado. The track of the near-surface vertical vorticity maximum is shown with a thin black line in each panel.

using dual-Doppler wind syntheses. The spatially averaged (within the circle) near-surface density potential temperature θ_ρ (Emanuel 1994) perturbation near the time of tornadogenesis is −3.5 to −4.0 K, and the virtual potential temperature θ_v perturbation is −2.0 to −2.5 K, roughly consistent with the minimum values near the tornadogenesis times of many F2+ tornadic storms examined by Markowski et al. (2002). Area-averaged updraft surrounding the tornado (Fig. 7b) and corresponding azimuthally averaged radial inflow relative to the axis of rotation (Fig. 8) near the time of tornadogenesis are consistent with the advection of angular momentum inward toward the axis of rotation. There are relative maxima of both updraft and downdraft within the mesocyclone at approximately 2155 and 2201 UTC (not shown), approximately corresponding to two tornado ΔV maxima during the genesis period (Fig. 1) and consistent with the strengthening, stalled, and restrengthening phases of the tornado and downdraft discussed in Kosiba et al. (2013). Consistent with the relatively warm outflow temperature during the tornadogenesis stage, the average CAPE (CIN and level of free convection, LFC) for parcels composing the near-surface outflow within the mesocyclone is relatively large (small) (Fig. 9), making it easier for low-level parcels to be accelerated upward (Markowski et al. 2003). Therefore, not only is downward acceleration due to negative buoyancy relatively small for parcels surrounding the low-level mesocyclone at this time, but these parcels have relatively large CAPE and low LFCs, making it easier for them to gain significant positive buoyancy aloft.

During the period of tornado intensification, the RFD surge strengthens and is closer to the center of rotation than at earlier times (Figs. 2c,d and 7b), yielding nearly zero or slight downward average vertical motion around the mesocyclone (it is nearly zero because both strong updraft and downdraft are present within the averaging area, configured in a pattern supportive of tornado intensification). Although low-level buoyancy and circulation decrease rather slowly as the tornado intensifies, their negative trends increase as the tornado reaches maturity, when the average near-surface air is about 3 K

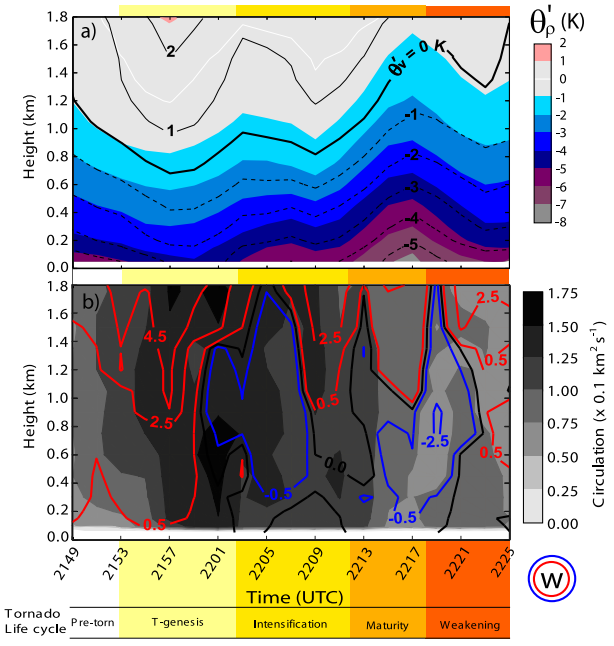

FIG. 7. (a) Ensemble-mean density perturbation potential temperature (shaded) and perturbation virtual potential temperature (contours) averaged within a 3-km-diameter circle centered on the maximum of ζ as a function of height and time. (b) Circulation (shaded) with respect to the peak of vertical vorticity at each height and mean vertical velocity (m s^{-1}; contours) as a function of height and time within the same 3-km-diameter circles. Red contours represent mean upward motion in the mesocyclone, blue contours represent mean descent, and black contours are neutral.

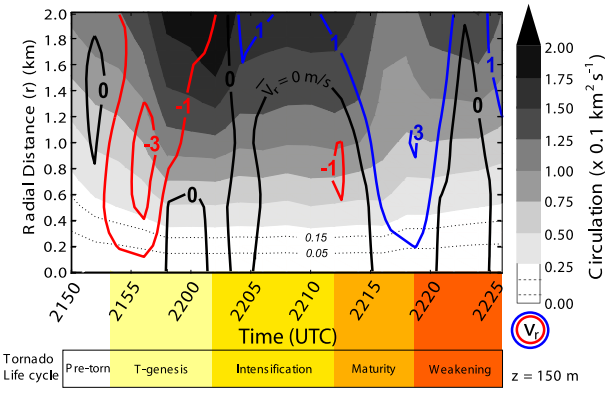

FIG. 8. As in Fig. 7b, but circulation is plotted as a function of radius from the center of circulation (vertical axis), and azimuthally averaged radial velocity (m s^{-1}; relative to the center of circulation) is contoured (red for inward and blue for outward velocity). All fields are valid at z = 150 m.

cooler than during tornadogenesis ($\theta'_\rho \sim -7$ K and $\theta'_v \sim -5$ K). These temperature perturbations are similar to those observed during the pretornadic stages of weakly tornadic storms and at the time of tornadogenesis failure in nontornadic storms in Markowski et al. (2002). The average CAPE of parcels composing the near-surface mesocyclone during tornado intensification is 25% less than that during the tornadogenesis stage. Average CIN increases by 35% over this time, and average LFC increases by 10% (Fig. 9). The convective potential of these outflow parcels decreases further during the period of tornado maturity (CAPE decreases an additional 15% and CIN and LFC both increase an additional 15%), and the standard deviation of these quantities among the samples of parcels decreases, indicating that the thermodynamic properties within the mesocyclone are becoming more homogenous. The reduced buoyancy and increased LFC of the air implies a more negative contribution to the vertical acceleration of near-surface outflow parcels surrounding the tornado, and any such parcels undergoing a dynamically forced vertical acceleration will be less likely to achieve strong vertical velocity.

Low-level buoyancy increases during the tornado weakening stage, and mean vertical velocity is near zero within the mesocyclone rather than negative. The average downdraft and divergence in the low-level mesocyclone are strongest during the transition between the mature and weakening phases of the tornado, coincident with a temporary decrease in the mesocyclone-scale circulation (Figs. 7b, 8). These temporary but distinct minima in circulation and vertical velocity correspond to the time when DOW7 undeployed. Given its close proximity to the mesocyclone and tornado at this time (~3 km), the cessation of assimilated DOW7 data might be expected to reduce the magnitude of the low-level vorticity and vertical velocity in our analyses (Supinie et al. 2016). However, DOW6 and NOAA X-band polarimetric (NOXP) radar data are assimilated during this time (Part I), each with lowest beam heights of approximately 170 and 300 m, respectively, and observations through midlevels. Although a brief change in the ensemble spread and root-mean-squared innovation (Dowell and Wicker 2009) for radar observations at this time suggests some response of the Kalman filter to this change in source data (Fig. 3 from Part I), depths over which mobile and WSR-88D observations are assimilated suggests that mid- and low-level EnKF vorticity analyses are qualitatively realistic. Therefore, it is unclear to what degree bulk trends in analysis variables at this time are due to changes in radar data sources or to the evolution of the storm that is transitioning between its mature and weakening tornadic phases. Although a rapid increase (decrease) of CAPE (CIN and LFC) at this time could be partly due to a transition in assimilated radar data sources and their influence on other variables via EnKF assimilation, the

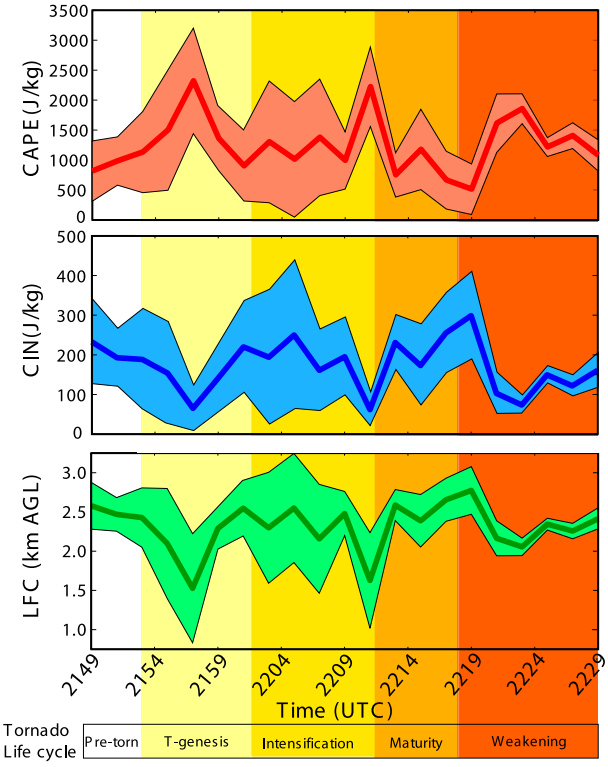

FIG. 9. CAPE, CIN, and LFC of parcels within the low-level mesocyclone throughout the life cycle of the tornado. Values are calculated by interpolating ensemble-mean temperature and vapor mixing ratio to 20 points evenly spaced along rings with a diameter of 1 km centered on the vertical vorticity maximum at $z = 200$ m at each analysis time. Interpolated temperatures and vapor mixing ratios at each point are then substituted into the base-state sounding at $z = 200$ m, the level from which CAPE, CIN, and LFC are calculated. Bold lines indicate the average, and the shaded regions indicate values within one standard deviation using the 20 points at each analysis time.

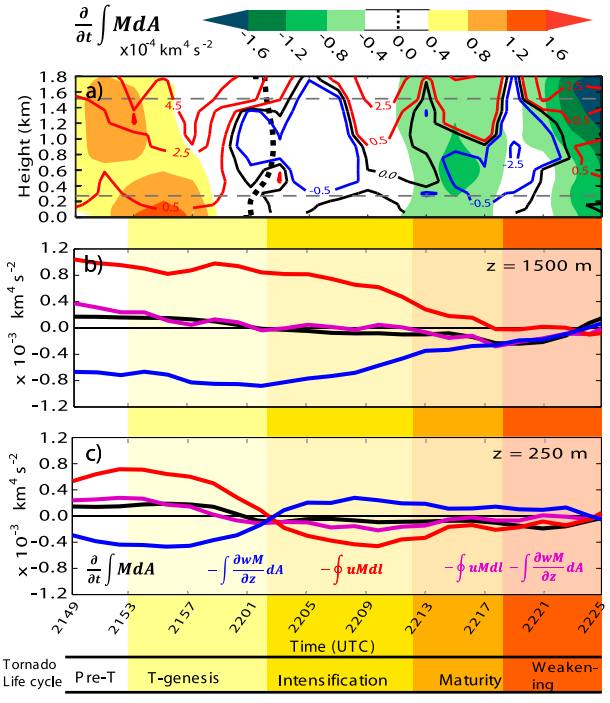

FIG. 10. (a) As in Fig. 7b, but $\partial/\partial t \int M\,dA$ is shaded (the 0.0 contour is shown as a thick dashed line). (b) Time series of $\partial/\partial t \int M\,dA$ (black), $-\oint uM\,dl$ (radial flux convergence of M; red), $-\int(\partial wM/\partial z)\,dA$ (vertical flux convergence of M; blue), and the sum of the radial and vertical flux convergence terms (purple; shown to illustrate budget reconciliation; cf. purple and black lines) along the periphery of or within the area encompassed by a 3-km-wide disk centered on the circulation maximum at $z = 1.5$ km. (c) As in (b), but at $z = 250$ m.

persistent assimilation of mobile mesonet observations to constrain the thermodynamic analyses in the outflow suggests that trends in these metrics are relatively robust compared to purely kinematic EnKF analyses.

Following Markowski et al. (2012b), we analyze the angular momentum M budget,

$$\frac{\partial}{\partial t}\int M\,dA = -\oint uM\,dl - \int \frac{\partial wM}{\partial z}\,dA, \qquad (1)$$

within the mesocyclone at each analysis time (Fig. 10), using vortex-relative winds in cylindrical coordinates, with u representing the radial wind. The lhs represents the rate of change of M within a circular horizontal disk (with radius of 1.5 km) centered on the circulation maximum. The terms on the rhs represent the radial and vertical flux convergence of M. Low-level radial M-flux convergence is present during the pretornadic and tornadogenesis stages, contemporaneous with mean updraft through the low-level mesocyclone (e.g., Figs. 10a, c). This pattern is consistent with an inward (toward the axis of rotation) and upward flux of M through the mesocyclone. Although the vertical flux divergence decreases M, this is more than offset by the inward radial flux. This finding is qualitatively consistent with the analysis of M surrounding the Dimmitt, Texas, tornado analyzed by Rasmussen and Straka (2007). The inward and upward flux trend is reversed later in the life cycle of the Goshen tornado, when radial M-flux divergence consistent with downward and outward transport of M is present near the ground (e.g., Fig. 10c). However, the downward and outward flux of M is only evident below ~1.5 km during tornado intensification; radial M-flux convergence and updraft are present above this height throughout tornado maturity (cf. Figs. 10b,c). Wakimoto et al. (2012) show divergence below $z = 500$–750 m during the maturity stage at 2216–2218 UTC using dual-Doppler data,[6] which may

[6] Their analyses are shown up to approximately 750 m.

qualitatively agree with the drop to near-zero radial M-flux convergence near 2218 UTC at $z = 1.5$ km in our EnKF analyses (Fig. 10b). It is unclear what physical process in our analyses a height-differential radial flux convergence denotes, but it may indicate a decoupling of the mid- and low-level mesocyclone and updraft. Regardless, it is interesting that the drop to a neutral or negative $\partial/\partial t \int M\, dA$ near the ground happens during the intensification stage of the tornado rather than during the transition from the maturity to weakening phases (Fig. 10c).

Atkins et al. (2012) note that dual-Doppler-estimated low-level circulation increases between 2158–2206 UTC, when downward and outward flow is measured, and conclude that the eddy flux of angular momentum might have been sufficient to intensify the tornado despite outward advection of M. However, their conclusions may be subject to unobserved near-surface convergence that could also intensify or maintain the tornado. It is difficult to confirm Atkins et al.'s eddy flux hypothesis with our EnKF analyses. However, the low-level radial gradient of circulation and average vertical motion in our analyses decreases starting in the tornado intensification period and becomes much more diffuse by the maturity period, qualitatively consistent with the Atkins et al. dual-Doppler observations. As noted above, there is an ~8-min lag between peak tornado intensity and peak near-surface mesocyclone-scale vorticity in the EnKF analyses. There is a similar amount of lag between peak mesocyclone vorticity and circulation. Thus, the lag between the peak in near-surface mesocyclone circulation and peak tornado ΔV is ~15 min. This suggests that there is not a strong correlation between the intensity of the tornado and changes in the pool of M surrounding it. Atkins et al. (2012) show a similar disagreement between dual-Doppler-estimated trends of M and tornado strength during the tornado intensification period.

5. Trajectory analysis

a. Flow through the mesocyclone

To illustrate changes in the flow through the low-level mesocyclone surrounding the tornado, trajectories are calculated for several sets of parcels passing through a 2-km-wide ring centered on the low-level ($z = 200$ m) vertical vorticity maximum throughout the life cycle of the tornado (Fig. 11). The trajectories are calculated backward (Figs. 11a,c,e,g) and forward (Figs. 11b,d,f,h) from their positions along the rings using the ensemble-mean u, v, and w analyses with a fourth-order Runge–Kutta scheme and interpolation performed at 10-s time steps between our 2-min EnKF analysis interval. This ring radius was chosen based on sensitivity tests described in Part I to reduce errors associated with intense accelerations in zones of large velocity gradients.

Parcels entering the low-level mesocyclone (i.e., approaching the 2-km-wide ring) at each time follow qualitatively similar paths (Figs. 11a,c,e,g). The majority of the parcels travel from the inflow environment at low levels and traverse the forward-flank baroclinic zone en route to the mesocyclone. A few other trajectories either reside in the cold pool within or northwest of the precipitation core for most of the integration period or enter the mesocyclone more directly from the ambient inflow. In Part I, we suggest that the subset of trajectories coming more directly from the inflow is an artifact of the coarse temporal resolution of our analyses, as in Dahl et al. (2012); therefore, we neglect these trajectories from further analysis. However, overall, our trajectories are qualitatively similar to those calculated in other studies of the Goshen storm (e.g., Markowski et al. 2012a,b; Kosiba et al. 2013) and other supercells (e.g., Brandes 1981, 1984; Wicker and Wilhelmson 1995; Wakimoto et al. 1998; Dowell and Bluestein 2002; Mashiko et al. 2009; Noda and Niino 2010; Dahl et al. 2012).

Perhaps the most noteworthy difference between the sets of trajectories is the altitude to which they ascend within the mesocyclone. During the tornadogenesis stage, most parcels approach the ring at or near $z = 200$ m and subsequently ascend into the midlevel updraft as they circulate within the mesocyclone (Figs. 11a,b). However, as the tornado life cycle progresses, fewer parcels reach midlevel altitudes within the mesocyclone. In general, there is an increase in the number of parcels that are captured by the mesocyclone (i.e., those that remain within the mesocyclone during the remainder of the integration period once they enter it) early in each trajectory integration period. Such parcels experience net ascent during their first few minutes circulating within the mesocyclone before subsequently descending into their positions in each ring (Figs. 11c,e,g; the period during which parcels composing the ring at 2225 UTC approach and enter the mesocyclone is illustrated using a ground-relative reference frame in Fig. 12). Other parcels wrap around the center of the low-level circulation and become part of the rear-flank outflow south and southwest of it along the ring. Many of the parcels subsequently ascend to midlevels along the rear-flank gust front during the tornado intensification and maturity periods, but not until they are several kilometers separated from the tornado (e.g., Figs. 11d,f). However, by the time of tornado demise, none of the parcels, even those captured by the mesocyclone early in their trajectory integration periods, ascend any higher than to $z = 800$–1000 m (Figs. 11g, 12). Instead, the parcels ultimately descend to altitudes near

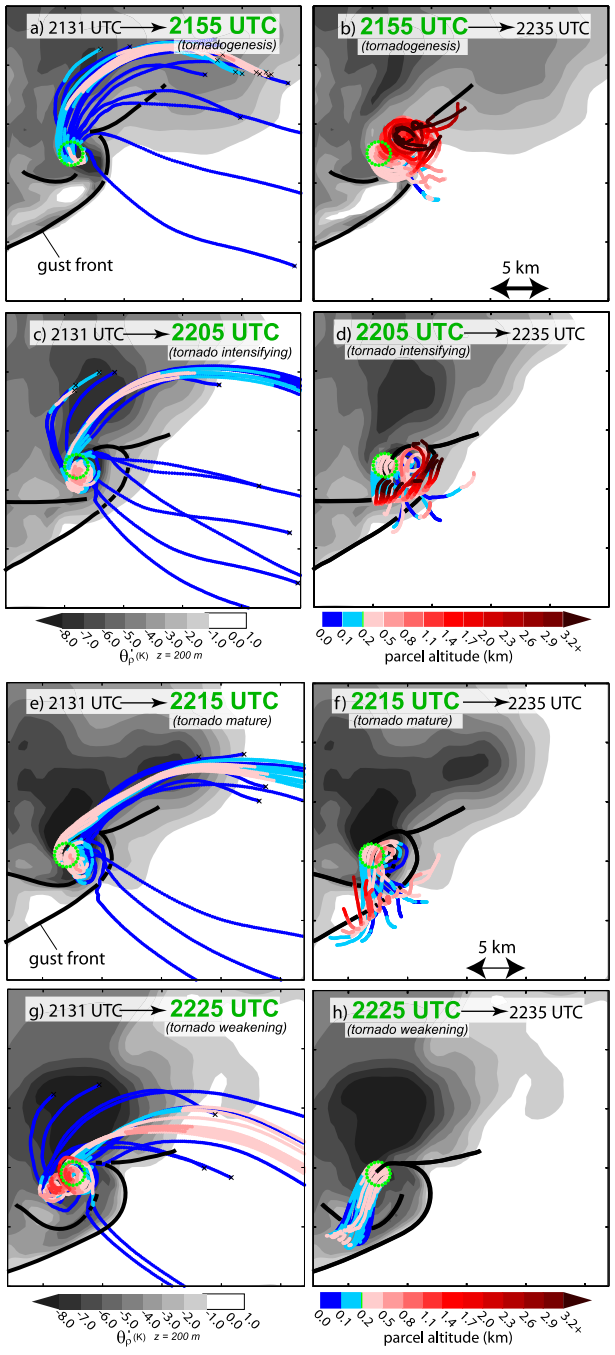

FIG. 11. Storm-relative trajectories of 20 parcels initially located 1 km from the maximum of ζ at $z = 200$ m (green dots) traced (a),(c),(e),(g) backward and (b),(d),(f),(h) forward in time during the (a),(b) formation; (c),(d) intensification; (e),(f) maturity; and (g),(h) weakening stages of the tornado. Dots along the trajectories are colorized according to parcel altitude above the ground level and are overlaid on ensemble-mean density potential temperature perturbation from the environment (shaded) and the near-surface gust front positions (thick black lines). Trajectories are traced back in time to 2131 UTC and forward in time to 2235 UTC.

the ground and travel southward, away from the mesocyclone (Fig. 11h).

We also analyze the flow through the midlevel mesocyclone by initiating backward trajectories within it to assess the physical processes connecting it to the low-level mesocyclone (Fig. 13). Although parcels composing most parts of the midlevel *updraft* throughout the life cycle of the tornado have similar origins in the ambient inflow environment (Figs. 13a,b), the paths taken by parcels passing through the midlevel *mesocyclone* (which, when defined as vertical vorticity $>0.01\,s^{-1}$, has a smaller horizontal cross section than the updraft in which it is embedded) differ as a function of time (Figs. 13c,d). Parcels passing through the midlevel mesocyclone at 2205 UTC (i.e., those ascending within the updraft during the formation–intensification stages of the tornado) can be summarized as following one of two typical trajectories (Fig. 13c). One common trajectory comes directly from the low-level inflow environment and ascends within the updraft near the intersection of the rear-flank gust front and forward-flank boundary. Along the second common trajectory, parcels are lifted directly out of the negatively buoyant low-level mesocyclone. However, none of the parcels passing through the midlevel mesocyclone at 2225 UTC (i.e., those ascending within the updraft during the mature–weakening stages of the tornado) are drawn from the low-level mesocyclone (Fig. 13d). Instead, midlevel mesocyclone parcels originate only from the low-level inflow environment and ascend abruptly in the low-level updraft at least 4–5 km horizontally separated from the tornado.

Although portions of trajectories within the mesocyclone or intense updraft may be prone to parcel position errors mentioned previously, overall, the vertical flows illustrated with the sets of trajectories shown in Figs. 11–13 are qualitatively consistent with the trends in average low-level vertical velocity shown in Fig. 7b. The trend of fewer outflow trajectories ascending into the midlevel updraft from within the low-level mesocyclone is consistent with the reduced upward accelerations that would accompany increasing negative buoyancy, CIN, and LFC of parcels within the low-level mesocyclone (Figs. 7a, 9). A lack of parcels within the low-level mesocyclone reaching midlevels during the maturity and weakening periods of the tornado is reminiscent of short vertical excursions observed in nontornadic mesocyclones, symptomatic of inadequate or diminishing low-level updraft that can intensify low-level vertical vorticity (Markowski et al. 2011). Most parcels within the low-level mesocyclone become part of the midlevel updraft during the tornadogenesis phase, when their negative buoyancy and CIN are relatively small. As a result, these parcels are more easily

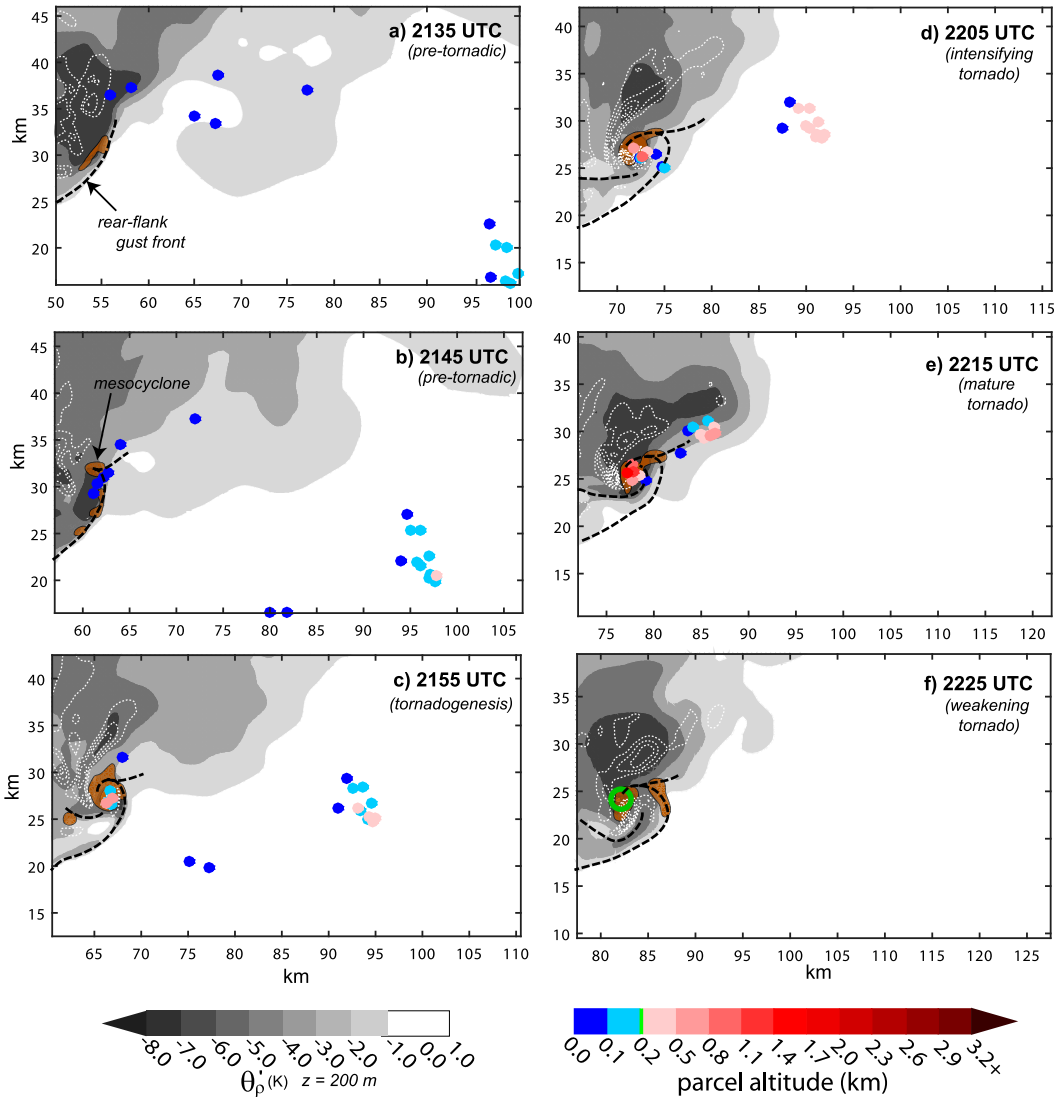

FIG. 12. As in Fig. 11g, but parcel positions and storm features are shown in a ground-relative frame at 10-min intervals between 2135 and 2225 UTC. Downdraft (white dashed contours; outermost is $-0.5\,\mathrm{m\,s^{-1}}$, incremented by $-0.5\,\mathrm{m\,s^{-1}}$) and vertical vorticity $> 0.005\,\mathrm{s^{-1}}$ (brown shaded area) at $z = 200\,\mathrm{m}$ are added for reference.

lifted to their relatively low LFCs, where they can subsequently realize their CAPE. As negative buoyancy and CIN increase, parcels are less easily lifted to their comparatively higher LFCs; thus, fewer parcels passing through the near-surface mesocyclone become part of the midlevel mesocyclone. The lack of parcels within the low-level mesocyclone reaching the midlevel mesocyclone could also result from a weak vertical perturbation pressure gradient force (VPPGF) and/or from the parcels exiting the low-level mesocyclone horizontally (e.g., Fig. 11h). Unfortunately, VPPGF analyses were not reliable in our experiments, as the pressure fields contained a significant amount of noise introduced during assimilation cycles (Potvin and Wicker 2013). Alternative methods for retrieving the three-dimensional pressure fields similar to Hane and Ray (1985), Potvin and Wicker (2013), and Skinner et al. (2015) yielded vertical gradients that were highly sensitive to the boundary conditions and other prescribed parameters necessary to numerically solve for them.

b. *Lagrangian vorticity budget analysis*

It was our goal to perform a quantitative assessment of vertical vorticity forcings along parcel trajectories entering the low-level mesocyclone throughout the life cycle of the tornado in order to evaluate the mechanisms for the formation and maintenance of

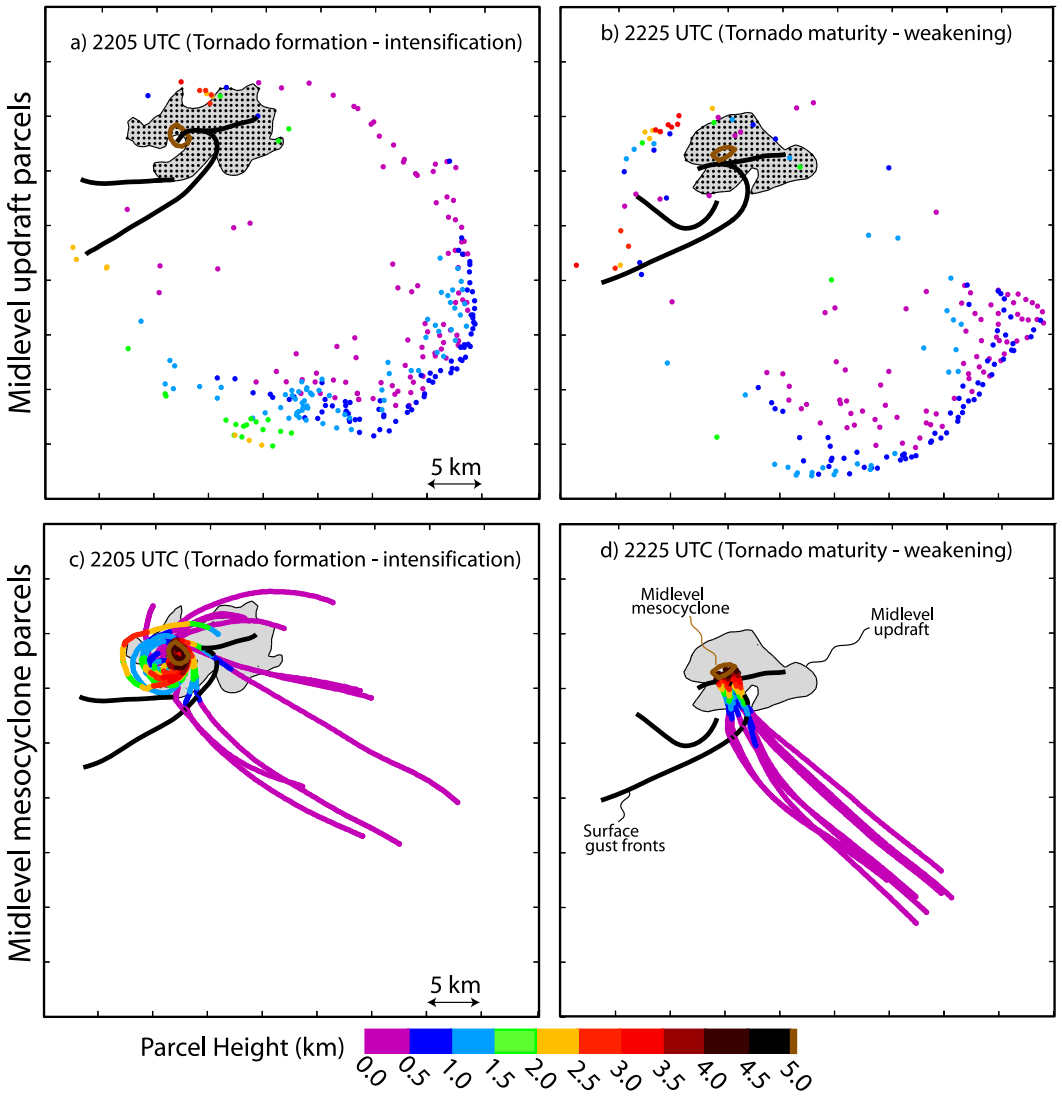

FIG. 13. (top) Locations of parcels at (a) 2135 and (b) 2155 UTC (colored dots) that compose the midlevel updraft at 2205 and 2225 UTC, respectively (i.e., all model grid points containing ensemble-mean $w > 10\,\mathrm{m\,s^{-1}}$ at $z = 5$ km; black dots within the gray shaded area in the upper left of each panel), determined using backward trajectory calculations. (bottom) Complete trajectories of each parcel passing through the midlevel mesocyclone (i.e., $\zeta \geq 0.02\,\mathrm{s^{-1}}$; brown contour) at (c) 2205 and (d) 2225 UTC. Colors of each dot indicate parcel altitude. Updrafts along near-surface gust fronts are traced with thick black lines. See Fig. 6 for relative placement of low- through midlevel mesocyclone and updraft.

near-surface rotation. However, vorticity tendency budgets calculated within the mesocyclone did not always reconcile well with the EnKF vorticity analyses, partly owing to errors in trajectory analysis as described in Part I and possibly owing to the simplification of using ensemble-mean fields to calculate vorticity forcings. Therefore, we limit our Lagrangian vorticity analysis to areas of the storm with less intense velocity gradients, such as within the forward-flank region. Parcels passing through this region en route to the mesocyclone develop significant horizontal vorticity that can be tilted into the vertical and stretched near the ground (e.g., Rotunno and Klemp 1985; Davies-Jones and Brooks 1993; Wicker and Wilhelmson 1995). Therefore, we seek to explore the relationship between changes in the horizontal vorticity of parcels entering the mesocyclone (defined herein as when parcels attain vertical vorticity of $0.01\,\mathrm{s^{-1}}$) and changes in tornado intensity.

Horizontal vorticity generated along a parcel trajectory is given by (neglecting viscous effects and tilting of planetary vorticity into the horizontal)

$$\xi(t) = \xi_0 + \int_{t_0}^{t} \left(\eta \frac{\partial u}{\partial y} + \zeta \frac{\partial u}{\partial z} + \xi \frac{\partial u}{\partial x} + \frac{\partial B}{\partial y} \right) dt',$$

$$\eta(t) = \eta_0 + \int_{t_0}^{t} \left(\xi \frac{\partial v}{\partial x} + \zeta \frac{\partial v}{\partial z} + \eta \frac{\partial v}{\partial y} - \frac{\partial B}{\partial x} \right) dt', \quad (2)$$

where (ξ_0, η_0) is the horizontal vorticity vector at the initial time of the forward trajectory, $B = g[(\theta_\rho - \overline{\theta_\rho})/\theta_\rho]$, and $\overline{\theta_\rho}(z)$ is the environmental density potential temperature. The first two terms in the integrands on the rhs represent tilting; the third term represents stretching; and the fourth term represents baroclinic production of horizontal vorticity. These calculations are performed along several sets of parcel trajectories approaching the low-level mesocyclone from the forward flank of the storm throughout the life cycle of the tornado (Fig. 14a). Parcel integration periods for these calculations vary depending on the span of time between initialization t_0 and the end of the ensemble spinup period (2131 UTC; discussed in Part I); thus, parcels approaching the mesocyclone during the weakening phase of the tornado have a longer integration period than those during the pretornadic phase. We omitted calculations from Fig. 14 for the parcels that are located close to the forward-flank baroclinic zone at 2131 UTC because they may not represent a full history of the influence of the forward-flank baroclinicity on the flow entering the low-level mesocyclone. Therefore, it is not expected that variation of integration periods of (2) significantly affects our analysis targeting vorticity production and residence time within the forward-flank baroclinic region.

The magnitude of the horizontal vorticity vector $[|\boldsymbol{\omega}_h| = |(\xi, \eta)|]$ is smallest for parcels entering the mesocyclone during the tornadogenesis period and increases as the tornado reaches maturity (white dots in Fig. 14a). The magnitude of the horizontal vorticity vector generated only by baroclinic processes [i.e., neglecting the tilting and stretching terms in (2); black dots in Fig. 14a], $|\boldsymbol{\omega}_h^{\mathrm{BC}}|$, contained by most parcels as they approach the mesocyclone follows a similar magnitude to that of $|\boldsymbol{\omega}_h|$,[7] indicating that, in the absence of frictional effects, the bulk of the horizontal vorticity is generated baroclinically. The mean magnitude of the horizontal buoyancy gradient $\overline{|\nabla_h B|}$ along each parcel trajectory entering the low-level mesocyclone is larger in the pretornadic, tornado maturity, and weakening stages than in the formation and intensification stages (Fig. 14c). Furthermore, the residence times of the

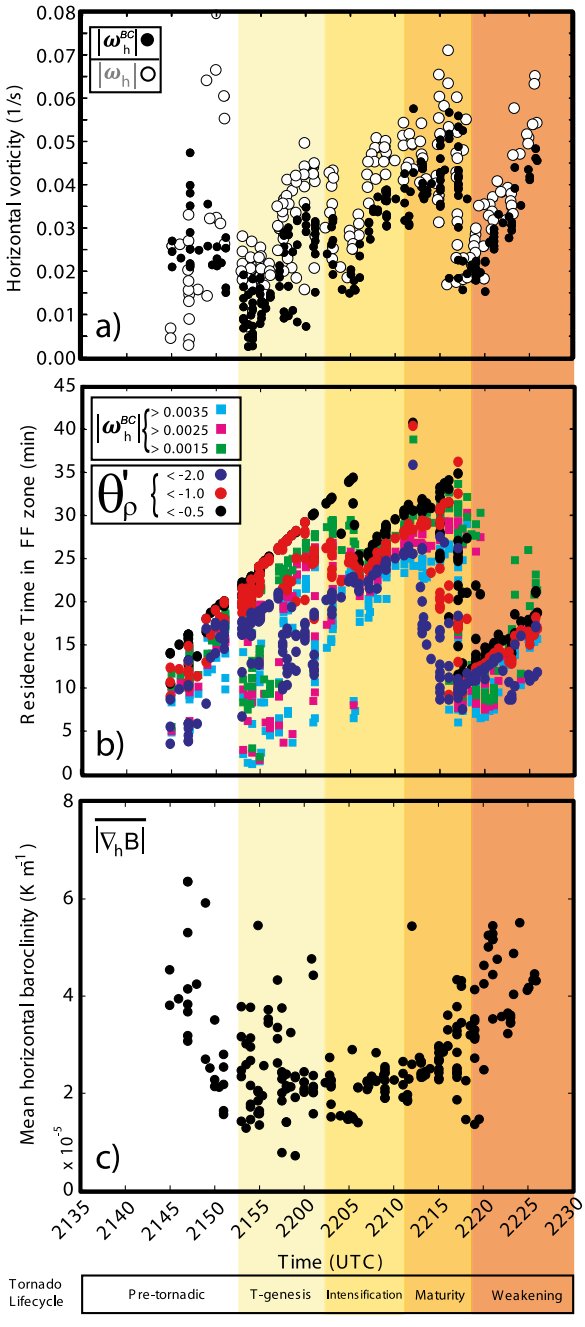

FIG. 14. (a) Magnitude of horizontal vorticity along trajectories of parcels passing through the forward-flank region of the storm and entering the mesocyclone between 2151 and 2229 UTC, calculated using (2) (white) and with only the baroclinic terms in (2) (black). Dots represent the value at the time when each parcel reaches the edge of the mesocyclone (when parcels contain 0.01 s^{-1}). (b) Residence time of the parcels in (a) within the forward-flank baroclinic zone of the storm estimated as the period during which parcels have a magnitude of baroclinically generated horizontal vorticity of at least (1.5, 2.5, or 3.5) $\times$ 10^{-3} s^{-1} or have a θ_ρ perturbation of at least -0.5, -1.0, or -2.0 K (i.e., the sensitivity of parcel residence times is tested using three different thresholds of two different metrics). (c) Average magnitude of the horizontal baroclinic gradient along the parcel trajectories in (a) within the forward flank of the storm.

[7] The far-field $\boldsymbol{\omega}_{\mathrm{BAROTROPIC}}$ points in approximately the same direction as $\boldsymbol{\omega}_{\mathrm{BC}}$ in the forward flank, in which case $|\boldsymbol{\omega}_h|$ can be approximated as $|\boldsymbol{\omega}_{\mathrm{BAROTROPIC}}| + |\boldsymbol{\omega}_{\mathrm{BC}}|$.

trajectories in the forward-flank region between the pretornadic and tornado maturity periods steadily increase (Fig. 14b). Horizontal vorticity that parcels are bringing to the low-level mesocyclone between tornado formation and maturity is increasing despite fewer parcels encountering strong horizontal B gradients (e.g., $>3 \times 10^{-5}\,\mathrm{K\,m^{-1}}$) because they are spending more time exposed to the forward-flank baroclinity.

There is an abrupt decrease of $|\boldsymbol{\omega}_h|$ and $|\boldsymbol{\omega}_h^{\mathrm{BC}}|$ for parcels approaching the low-level mesocyclone near the end of the period of tornado maturity. This transition occurs following a period when the areal extent of low-level forward-flank outflow decreases; the magnitude of the temperature deficit 10–20 km east-northeast of the mesocyclone decreases between ~2205 and 2210 UTC. As a result, parcels traveling through the forward-flank region after ~2210 UTC spend less time exposed to the baroclinity (Fig. 14b). However, the $\overline{|\nabla_h B|}$ closer to the mesocyclone increases shortly afterward, owing to much more negatively buoyant air being produced within the precipitation core; thus, the abrupt decrease in $|\boldsymbol{\omega}_h^{\mathrm{BC}}|$ at approximately 2215 UTC reverses during the tornado weakening period because those parcels reside in more intense baroclinicity (Figs. 14b,c). There are insufficient in situ observations available to verify the decreasing areal extent of cold forward-flank outflow far east-northeast of the mesocyclone between ~2205 and 2210 UTC. We assessed the sensitivity of this outflow warming to different radii of influence applied to the mobile mesonet observations and schemes for maintaining ensemble spread during data assimilation [e.g., adaptive inflation as in Anderson 2007; additive noise as in Dowell and Wicker (2009); and environmental perturbations as in Aksoy et al. (2009)], and different model microphysics parameterizations (see section 3 of Part I). Qualitative trends in $\overline{|\nabla_h B|}$ and forward-flank parcel residence times from such tests are similar to those shown herein.

Taken at face value, this vorticity analysis suggests a correlation between tornado intensity and the amount of baroclinically generated horizontal vorticity entering the low-level mesocyclone for much of the tornado life cycle (except during the late maturity and weakening phases). However, owing to our model grid resolution and assumptions made in these analyses, we expect the buoyancy, circulation, horizontal convergence, and trajectory calculations discussed above to more accurately describe trends in the mesocyclone-scale vorticity and circulation (resolved by the model grid), rather than the tornado-scale flow (unresolved). The relationship between the production of horizontal vorticity within the forward flank and the tendency of the mesocyclone circulation is ambiguous. Circulation is relatively large (small) during the period of tornado formation–intensification (maturity), when parcel $|\boldsymbol{\omega}_h|$ immediately upstream of the mesocyclone is smallest (largest) (cf. Figs. 7b and 14a). Furthermore, peak vertical vorticity within the near-surface mesocyclone occurs several minutes prior to the largest incoming horizontal vorticity (during the end of the tornado intensification period). This analysis may indicate that the low-level updraft/downdraft structure near the mesocyclone is less able to tilt the parcels with baroclinically generated horizontal vorticity during the period of tornado maturity than at earlier times despite there being more horizontal vorticity available. A disruption of the low-level updraft/downdraft structure owing to a combination of the surging secondary RFD and colder air from the main precipitation core circulating into the mesocyclone may have disrupted the tilting process. However, the tornado reaches its maximum strength when surrounded by the strongest low-level stretching of vertical vorticity (Fig. 4b) despite relatively weak tilting of horizontal vorticity and mesocyclone circulation.

There are possible caveats to this analysis. The mobile mesonets did not observe the outflow of the Goshen County storm until approximately 2140 UTC; therefore, the only influence they have on outflow temperature in the model ensemble prior to this is while they are in the near-storm environmental inflow within the prescribed 18-km horizontal radius of influence. Therefore, parcels traversing this region and approaching the mesocyclone prior to approximately 2155 UTC could be affected by an inaccurate shape or strength of the forward-flank baroclinicity. Furthermore, limiting our analysis only to the forward-flank region precludes understanding important details of tilting of horizontal vorticity in the downdraft when parcels are within the mesocyclone and in close proximity to the tornado (e.g., Davies-Jones and Brooks 1993).

6. RFD surge and secondary RFGF

We investigate the development of the RFD surge because of its possible influence on the formation of the tornado in this storm (Kosiba et al. 2013). The development of the surge is documented with a series of vertical cross sections along streamlines that pass southwest of the tornado at several times (Figs. 15, 16). In the early development of the surge, the vertical structure of the cold pool collocated with the outflow surge boundary assumes a shape common to many observations and simulations of density currents, with an elevated head leading colder air (Figs. 16a,b). As the surge strengthens, warmer air from above the cold pool is entrained into the outflow (Figs. 16a–c). By the start of the tornadogenesis period, continued downward transport and mixing of warm air from above into the colder air has eliminated the high density air

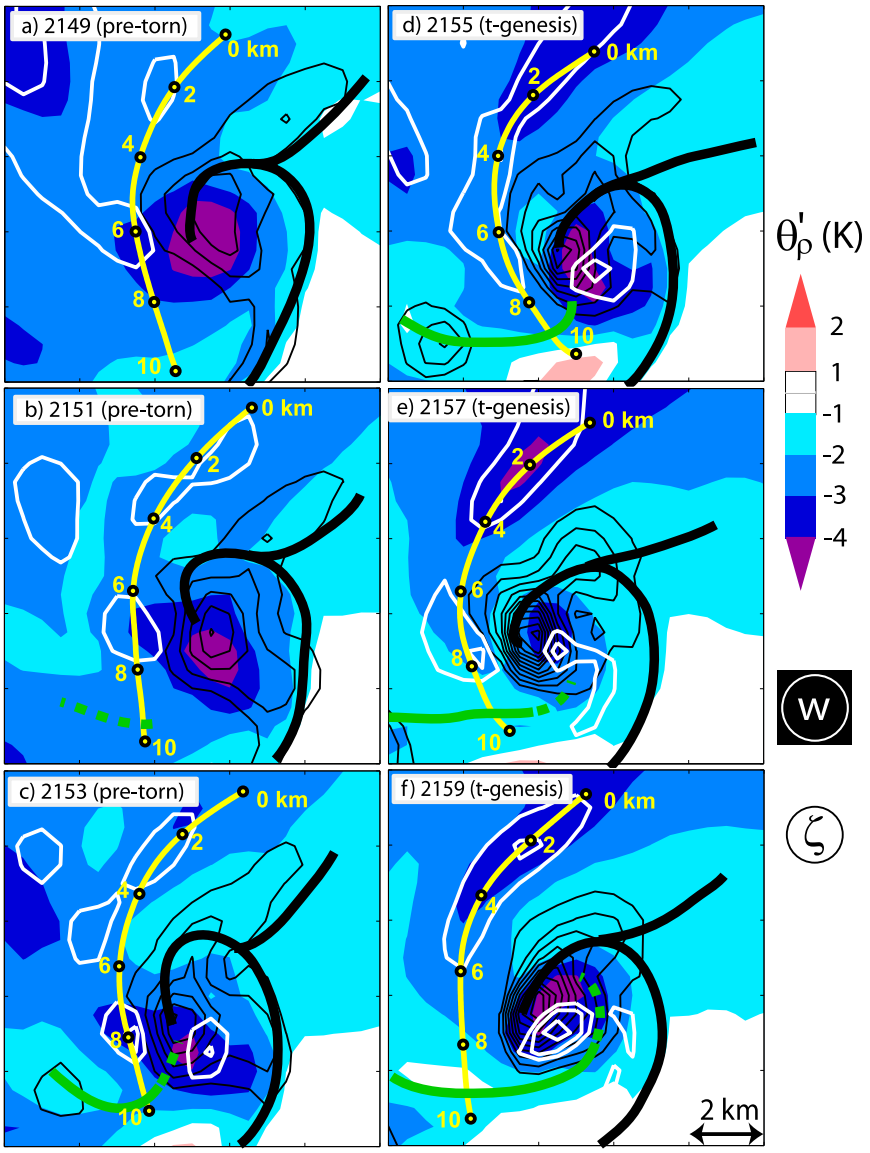

FIG. 15. Vertical vorticity (black contours; outermost is 0.005 s^{-1}, incremented by 0.005 s^{-1}), downdraft (white contours; outermost is -1 m s^{-1}, incremented by -1 m s^{-1}), θ_ρ perturbation (shaded), and traces of the updraft maximum along the rear-flank gust fronts (heavy lines) at z = 200 m throughout the development of the secondary rear-flank downdraft surge and gust front (black lines for the primary gust fronts and green lines for the secondary gust front). Yellow lines trace streamlines in each that pass through the rear-flank downdraft core along which vertical cross sections are shown in Fig. 16.

aloft, and the cold pool just southwest of the main low-level circulation (just upstream of the surge boundary) is much shallower and warmer than before (cf. $6 < x' < 8$ km in Fig. 16a and $6 < x' < 10$ km in Figs. 16d–f). Therefore, the development of the surge corresponds to a warming of the outflow air southwest of the mesocyclone and possibly the air within it during tornadogenesis (Fig. 7a).

To further investigate the origins of the RFD surge and buoyancy of the air composing it, we calculate backward trajectories of parcels initially located at model grid points immediately west, southwest, and southeast of the vertical vorticity maximum that contain $w < -1$ m s^{-1} at z = 200 m. Trajectories are traced backward from three times: (i) prior to the onset of the downdraft surge near the surface, (ii) shortly after it reaches the surface, and (iii) during the weakening of the tornado when the areal coverage of low-level downdraft has increased in the mesocyclone (Fig. 17). Prior to

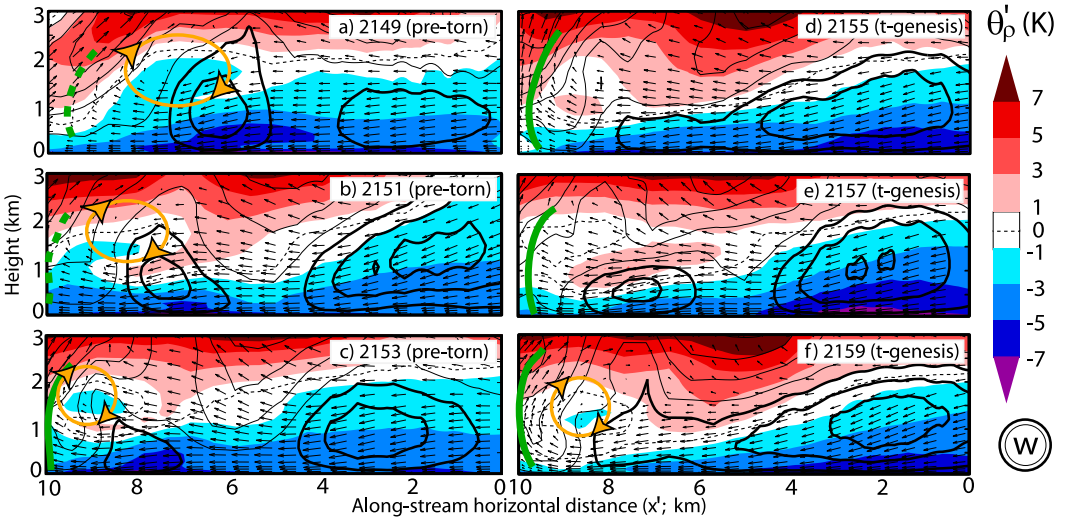

FIG. 16. Vertical cross sections of θ_ρ perturbation (shaded), downdraft (thick black contours; starts at $-1\,\mathrm{m\,s^{-1}}$, incremented by $-2\,\mathrm{m\,s^{-1}}$), updraft (thin black contours; starts at $1\,\mathrm{m\,s^{-1}}$, incremented by $3\,\mathrm{m\,s^{-1}}$), and the flow (vectors) along the yellow streamlines shown in Fig. 15. The secondary gust front is traced with heavy green lines. Orange circles indicate areas of mixing referred to in the main text.

the development of the RFD surge, parcels located in the area of broad downdraft several kilometers west of the mesocyclone have very similar trajectories during the ~20-min integration period. Most approach the storm from a variety of altitudes between 250 and 1600 m in the inflow environment, ascend a few hundred meters within updraft on the interface of the forward-flank outflow and the environment, and finally descend to $z = 200\,\mathrm{m}$ northwest of the mesocyclone center (Fig. 17a). Parcels are positively or neutrally buoyant

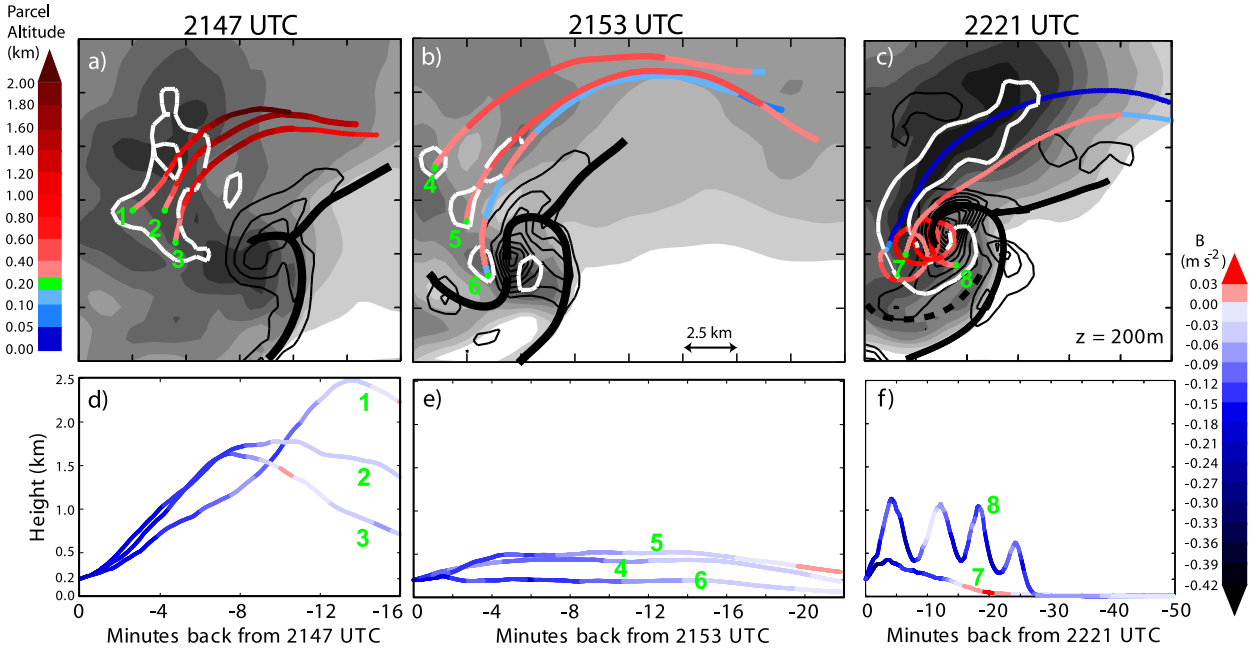

FIG. 17. (a)–(c) Select parcel trajectories traced backward in time from grid points containing the low-level ($z = 200\,\mathrm{m}$) rear-flank downdraft at 2147, 2153, and 2221 UTC. Parcel positions are colored according to altitude. Positive vertical vorticity and $w = -1\,\mathrm{m\,s^{-1}}$ are contoured (black and white, respectively; outermost vorticity contour is $0.004\,\mathrm{s^{-1}}$, incremented by $0.004\,\mathrm{s^{-1}}$). Updrafts along the near-surface gust fronts are traced with thick black lines. Perturbation θ_ρ at $z = 200\,\mathrm{m}$ is gray shaded (the interface between white and the first gray shade is the -1-K contour, incremented by $-1\,\mathrm{K}$). (d)–(f) Altitude of the parcels in (a)–(c) as a function of time. Trajectories are colored according to parcel buoyancy.

during their ascent and become negatively buoyant shortly before their descent (Fig. 17d). This indicates that evaporation and melting of hydrometeors and precipitation loading likely played a key role in the production of the downdraft. However, we reiterate that there is uncertainty in the reliability of the EnKF precipitation analyses because radar reflectivities derived from them were larger overall than those observed by the nearest WSR-88D (see Part I).

Parcels composing the RFD surge developing a few minutes later (Fig. 17b) follow similar qualitative paths to those discussed previously, except that they descend from much lower altitudes. Most of these parcels descend from $z < 600$ m (Fig. 17e), gaining negative buoyancy while in the forward-flank precipitation. Trajectories terminating within the near-surface RFD immediately west of the mesocyclone ascend slightly from near the surface within the ambient inflow, but undergo virtually no descent while within the storm.

Most parcels composing the near-surface downdraft located west and south of the mesocyclone after the initial development of the surge follow two common trajectories (e.g., Fig. 17c). One of these trajectory types, common among those terminating in the RFD west and southwest of the mesocyclone (e.g., parcel 7 in Fig. 17), originates from the inflow environment, ascends a few hundred meters in the forward-flank region, and becomes negatively buoyant within the precipitation prior to its descent. Along a second common trajectory (e.g., parcel 8 in Fig. 17), parcels arrive at the mesocyclone from altitudes near the surface. Their altitudes oscillate as they circulate within the mesocyclone, rising within the low-level updrafts north of the circulation center and along the RFD surge gust front and descending within the RFD. It is unclear whether this trajectory pattern is an artifact of the relatively coarse temporal resolution of our EnKF analyses or if it is an accurate depiction of parcels experiencing no net ascent as they circulate within a mesocyclone that is composed of updraft and downdraft. If accurate, this pattern indicates that many parcels within the near-surface downdraft are recycled from within the mesocyclone, perhaps similar to motions derived from photogrammetric analyses of tornadoes by Fujita (1975). Trajectories similar to parcel 8 in Figs. 17c,f are quite negatively buoyant throughout their vertical oscillation within the mesocyclone, as are others approaching the mesocyclone prior to experiencing significant descent (e.g., parcels 4–7). Such patterns suggest that VPPGFs are an important term in their vertical momentum budgets (as in Skinner et al. 2015). Although the influence of VPPGFs on the surging downdraft could not be determined quantitatively from our analyses, the descent of relatively warm air into the cold outflow south-southwest of the mesocyclone (Fig. 16) suggests that they could play a role in the formation of the RFD surge in this storm. The large downdraft that surrounds most of the dissipating mesocyclone (Figs. 2e,f) is composed of parcels following a combination of the two typical trajectories shown in Fig. 17c; thus, the downdraft associated with tornado dissipation may result from a combination of negative buoyancy and VPPGFs. It is possible that the increasing negative buoyancy of the RFD air throughout tornado intensification and maturity periods is due to changes in the evaporation rates associated with changes in the observed raindrop size distributions (French et al. 2015), but this effect cannot be confirmed in the present analysis because the simulations' single-moment microphysics parameterization does not vary the drop size distribution.

7. Discussion

Definitive conclusions about how changes in the storm-scale and mesocyclone-scale flow and outflow buoyancy affect the tornado are not possible because the tornado is not explicitly resolved in our simulations. However, there are a few interpretations of our results that are consistent with past studies.

Changes in tornado intensity are related to changes in the radial distribution of angular momentum; thus, the presence of strong low-level circulation, radial convergence, and only weakly negatively buoyant outflow air during the period of tornadogenesis in our analyses is perhaps intuitive and consistent with past studies (e.g., Markowski et al. 2003). Comparing radar observations of low-level circulation within four mesocyclones to three others studied in Markowski et al. (2011), Marquis et al. (2012) noted that the pool of angular momentum was not necessarily stronger in the tornadic mesocyclones than in nontornadic ones. Multi-Doppler radar wind synthesis estimates of low-level circulation at $r = 1.8$ km in the Goshen storm are ~ 1–1.5×10^5 m^2 s^{-1} (Atkins et al. 2012), values ranging between strongly and weakly tornadic mesocyclones in Marquis et al. (2012) and similar to the values for nontornadic cases in Markowski et al. (2011).[8]

[8] These may not be compared at consistent times relative to the life cycle of each tornado; Marquis et al. (2012) focused on the tornado maturity and weakening periods, and Markowski et al. (2011) focused on what was presumed to be near the time of tornadogenesis failure in nontornadic supercells. Marquis et al. (2014b) compare angular momentum calculations from the EnKF analyses of the Goshen storm presented herein to similar ones from two other tornadic cases examined in Marquis et al. (2012), showing that the Goshen mesocyclone had a similar circulation to another containing a much weaker and shorter-lived tornado (Argonia, Kansas) and had larger circulation overall than another containing an equally strong and long-lived tornado (Almena, Kansas).

Markowski et al. (2011) concluded that sustained low-level convergence collocated with a pool of angular momentum was a necessary condition for tornadogenesis. Marquis et al. (2012) concluded that the maintenance of tornado intensity is more closely related to the evolving low-level mesocyclone-scale radial convergence than to the strength of the circulation of the mesocyclone. However, decreasing circulation and outflow buoyancy and average downdraft within the Goshen mesocyclone as the tornado intensifies and matures is perhaps counterintuitive. Although peak near-surface vertical vorticity within the mesocyclone was better correlated with peak tornado intensity in the Goshen case, the sizable lags between peak low-level mesocyclone circulation, vertical vorticity, and peak tornado intensity suggest that smaller-scale maxima in vertical vorticity only require a minimum pool of surrounding angular momentum to advect inward toward the axis of rotation via radial convergence. Mean low-level updraft and convergence present during the tornadogenesis phase is consistent with the Marquis et al. (2012) findings. However, mean low-level downdraft and near-zero horizontal convergence at small radii from the center of the mesocyclone during the tornado intensification and maturity periods is not. Therefore, reconciliation of the Marquis et al. (2012) findings with the tornado intensification and maturity period in the present case is unclear and may be a result of a coarser spatial resolution used in our model than in their dual-Doppler grids or missing low-level convergence in the assimilated wind fields. A finer model resolution is likely needed to capture small regions of updraft in which parcels are lifted directly into the tornado and their vorticity is stretched to tornadic intensity.

Several studies have illustrated the potential importance of horizontal convergence and vertical vorticity generated along a secondary rear-flank gust front within a mesocyclone (e.g., Wurman et al. 2007; Marquis et al. 2008, 2012; Skinner et al. 2014). Kosiba et al. (2013) hypothesize that the RFD surge and convergence along the attendant gust front enhanced both the tilting of horizontal vorticity baroclinically generated in the outflow and the stretching of vertical vorticity surrounding the Goshen tornado. Trajectories of parcels surrounding the tornado in our simulations followed qualitatively similar paths and reveal similar processes generating the horizontal vorticity in the forward flank of the storm, as shown in Kosiba et al. (2013) and Markowski et al. (2012a,b), despite resolution differences between our analyses. Therefore, our results are consistent with the idea that locally enhanced tilting and stretching of vorticity within the updraft/downdraft associated with the RFD surge and its gust front enhances vertical vorticity within the larger pool of mesocyclone-scale angular momentum. However, limitations in the spatial and temporal resolution of our analyses make it difficult to confirm this process.

It is interesting to note the qualitatively similar structure and kinematic evolution of RFD surges and gust fronts among various storms in the recent literature containing tornadoes of different peak intensity (e.g., Wurman et al. 2007, 2010; Marquis et al. 2012; Kosiba et al. 2013). Similar observations are made in non- or marginally tornadic supercells (e.g., Skinner et al. 2014), although there are fewer examples in such storms in the literature. The spatial scales of the RFD surges and gust fronts typically are much larger than that of a typical tornado, suggesting that a larger-scale feature is responsible for their formation. However, despite their kinematic similarities, there have been observations of positive, negative, and neutral horizontal buoyancy gradients reported across secondary gust fronts (Lee et al. 2004a,b, 2008, 2012; Marquis et al. 2012; Kosiba et al. 2013). VPPGFs have been shown to be significant terms in the vertical momentum budgets in supercell storms, particularly at low levels (e.g., Klemp and Rotunno 1983; Wicker and Wilhelmson 1995; Skinner et al. 2015; Schenkman et al. 2016). Therefore, VPPGFs could be a common forcing of RFD surges across supercell storms. The role of VPPGFs can be only speculated in the present case owing to inaccurate pressure analyses; therefore, the relative role of downward acceleration from negative buoyancy in the Goshen RFD surge is unclear. However, descent of positively buoyant air from aloft into the colder outflow air suggests that VPPGFs may have played a role in the RFD surge.

Other studies have indicated that certain small-scale features perhaps not well represented in our model could be important to the Goshen tornado. For example, Markowski et al. (2012a,b) indicate that a descending reflectivity core (DRC) may have been associated with an increase in low-level angular momentum prior to tornadogenesis. Although a DRC is not present in our analyses, our ensemble does reproduce the increase in low-level circulation at that time owing to the assimilation of radar velocity data. Therefore, all processes causing the increase in circulation may not be represented in our analyses even if the circulation is accurately reproduced. Richardson et al. (2012) hypothesize that patches of vertical vorticity forming along finescale spiraling rainbands that are ingested by the Goshen tornado may help to maintain it. Furthermore, they hypothesize that dissipation of the tornado occurs as a particular band of precipitation falls close to the axis of rotation. Neither of these features are well represented on our model grid; therefore, we cannot comment on their roles in modifying the tornado. The effects of particle centrifuging on the

divergence field surrounding the tornado are assumed small in our analyses because of the relative small size of the tornado and the smoothing applied to the observations before they are assimilated to our model grid. Our freeslip lower boundary condition precludes assessing the influence of friction on the mesocyclone. We also cannot explore the range of tornado-scale intensification and corner flow properties for a given mesocyclone-scale circulation and convergence, as discussed in Lewellen et al. (2000), owing to the fact that the tornado is not resolved in our simulations. Therefore, a tornado could form and intensify or weaken owing to a combination of finescale aspects of the flow not represented in this study.

8. Conclusions

A variety of storm-scale and mesocyclone-scale processes in the Goshen County, Wyoming, tornadic supercell observed during VORTEX2 were examined using the ensemble analyses produced with EnKF data assimilation described in Part I of this study. We focused on relationships among changes in three-dimensional storm morphology, a surging rear-flank downdraft, updraft and circulation within the low-level mesocyclone, baroclinicity, and tornado intensity to examine how the tornado-scale flow is affected by the evolving larger-scale flow (summarized in Fig. 3).

Tornadogenesis occurred within a low-level mesocyclone that was relatively warm (albeit, negatively buoyant) compared to other times, with relatively high (low) CAPE (CIN and LFC) and enhanced circulation collocated with azimuthally averaged near-surface horizontal convergence and updraft (Figs. 7–9). Thermodynamic and kinematic analyses surrounding the mesocyclone suggest that processes generating a rear-flank downdraft surge may have resulted in a warming of the low-level outflow at the time of tornadogenesis (Fig. 16), likely assisting with the enhancement of low-level updraft and vertical vorticity. Buoyancy and circulation all decreased within the mesocyclone after tornadogenesis, and mean vertical velocity became slightly negative because of a stronger downdraft surrounding the intensifying and mature tornado than during previous times (albeit, updraft is present still within the mesocyclone). Air within the mesocyclone was most negatively buoyant as the tornado reached maturity (EF2 intensity). Buoyancy increased slightly, and average vertical velocity was near zero during the weakening phase of the tornado; however, circulation and vertical vorticity within the mesocyclone decreased.

The majority of the parcel trajectories passing through the low-level mesocyclone throughout the life of the tornado traveled through the forward-flank region of the storm; therefore, there were not significant changes to the origins of air surrounding the tornado (Fig. 11). Parcels within the low-level mesocyclone were drawn upward into the primary midlevel updraft and mesocyclone during tornado formation but were not during subsequent periods of the tornado life cycle. Although accurate dynamically driven vertical perturbation pressure gradient forces could not be diagnosed from the EnKF analyses, our results imply that upward-pointing perturbation pressure gradient forces were sufficient to lift weakly negatively buoyant air from within the mesocyclone at the time of tornadogenesis but insufficient to overcome the quite negatively buoyant air surrounding the mature tornado. We hypothesize that, although many of the parcels surrounding the tornado at these later times contained $>500\,\mathrm{J\,kg^{-1}}$ CAPE (albeit lower than previous times), their CIN and LFC increased sufficiently (~25%–35%) to retard the low-level updraft from drawing in outflow. Therefore, decoupling of the low-level and midlevel mesocyclone and updraft occurred when more strongly negatively buoyant outflow and downdraft occupied more area within the mesocyclone than at prior times, disrupting the previous storm-scale updraft/downdraft structure at low levels that was supportive of the tornado.

The amount of horizontal vorticity generated within the forward flank of the storm available to be tilted at low levels changed throughout the life of the tornado and better corresponded to tornado intensity (except during the end of the tornado maturity period) than to the magnitude of vertical vorticity or circulation associated with the mesocyclone (Fig. 14). It is unclear if the correspondence between tornado intensity and the amount of horizontal vorticity contained by parcels approaching the mesocyclone is coincidental, owing to our model resolution. The lack of a clear relationship between vertical vorticity or circulation within the mesocyclone and parcel horizontal vorticity may indicate that there need only be a minimum amount of vertical vorticity produced through tilting to be stretched by low-level updraft to support the tornado. That amount, which might depend on the magnitudes of the low-level updraft, buoyancy, and horizontal updraft gradient, is unclear based on this study.

The model grid resolution and simplifications employed by this study (owing to computational limitations) precluded a complete understanding of the interaction between tornado-scale flow and larger-scale processes occurring within the storm. As a result, several important questions have arisen about the interaction between these scales that could not be definitively answered in the present analysis:

1) How general are the relationships between tornado intensity and larger-scale vertical velocity, circulation, and buoyancy within the mesocyclone from the

present case to a larger number of tornadic supercells? Do processes causing and maintaining the tornado occur only on spatial scales much smaller than the mesocyclone?

2) How do changes in production of baroclinic vorticity and its reorientation along parcel trajectories entering the mesocyclone influence tornado evolution? Is there a minimum amount of horizontal vorticity necessary to generate the near-surface mesocyclone and tornado via tilting (and subsequent stretching)?
3) Are the processes causing RFD surges similar across many supercells? What are the relative roles of negative buoyancy (including descending reflectivity cores) and VPPGFs in RFD formation before and during surges?

Answering these questions will require a fine-resolution grid nested within a cloud-resolving simulation, possibly employing a more complex model than that used in the present study (e.g., surface physics and heterogeneous environment). As shown in Part I, assimilation of high-resolution kinematic and thermodynamic observations can reduce uncertainty in the analyses that results from the use of simplified model parameterizations (e.g., microphysics schemes). Therefore, decreased model uncertainty owing to the assimilation of more high-resolution observations in additional supercells may improve our understanding of the interactions between storm-scale processes and the tornado-scale flow.

Acknowledgments. This research was funded by National Science Foundation Grants AGS-0801035, AGS-0801041, AGS-1157646, AGS-1211132, AGS-1361237, and AGS-1447268. Simulations were conducted using NCAR CISL supercomputing facilities (Yellowstone), and NCAR DART and WRF-ARW software packages. We wish to thank David Dowell, Glen Romine, Nancy Collins, Jeff Anderson, Johannes Dahl, Dan Dawson, Lou Wicker, Hugh Morrison, George Bryan, Chris Snyder, Don Burgess, Tony Reinhart, Terra Ladwig, Robin Tanamachi, Matt Parker, Chris Weiss, and Morris Weisman for helpful discussion of topics related to this research. We also thank Patrick Skinner and two anonymous reviewers for their constructive comments and suggestions, and all participants of VORTEX2 for their dedication in collecting the data used in this study.

REFERENCES

Aksoy, A., D. C. Dowell, and C. Snyder, 2009: A multicase comparative assessment of the ensemble Kalman filter for assimilation of radar observations. Part I: Storm-scale analyses. *Mon. Wea. Rev.*, **137**, 1805–1824, doi:10.1175/2008MWR2691.1.

Alexander, C., and J. Wurman, 2008: Updated mobile radar climatology of supercell tornado structures and dynamics. *24th Conf. on Severe Local Storms*, Savannah, GA, Amer. Meteor. Soc., P19.4. [Available online at https://ams.confex.com/ams/24SLS/techprogram/paper_141821.htm.]

Anderson, J. L., 2007: An adaptive covariance inflation error correction algorithm for ensemble filters. *Tellus*, **59A**, 210–224, doi:10.1111/j.1600-0870.2006.00216.x.

Atkins, N. T., A. McGee, R. Ducharme, R. M. Wakimoto, and J. Wurman, 2012: The LaGrange tornado during VORTEX2. Part II: Photogrammetric analysis of the tornado combined with dual-Doppler radar data. *Mon. Wea. Rev.*, **140**, 2939–2958, doi:10.1175/MWR-D-11-00285.1.

Beck, J., and C. Weiss, 2013: An assessment of low-level baroclinicity and vorticity within a simulated supercell. *Mon. Wea. Rev.*, **141**, 649–669, doi:10.1175/MWR-D-11-00115.1.

Brandes, E. A., 1981: Finestructure of the Del City-Edmund tornadic mesocirculation. *Mon. Wea. Rev.*, **109**, 635–647, doi:10.1175/1520-0493(1981)109<0635:FOTDCE>2.0.CO;2.

——, 1984: Vertical vorticity generation and mesoscyclone sustenance in tornadic thunderstorms: The observational evidence. *Mon. Wea. Rev.*, **112**, 2253–2269, doi:10.1175/1520-0493(1984)112<2253:VVGAMS>2.0.CO;2.

Dahl, J. M., M. D. Parker, and L. J. Wicker, 2012: Uncertainties in trajectory calculations within near-surface mesocyclones of simulated supercells. *Mon. Wea. Rev.*, **140**, 2959–2966, doi:10.1175/MWR-D-12-00131.1.

Davies-Jones, R., and H. E. Brooks, 1993: Mesocyclogenesis from a theoretical perspective. *The Tornado: Its Structure, Dynamics, Prediction, and Hazards, Meteor. Monogr.*, No. 79, Amer. Meteor. Soc., 105–114.

Dowell, D. C., and H. B. Bluestein, 2002: The 8 June 1995 McLean, Texas, storm. Part II: Cyclic tornado formation, maintenance, and dissipation. *Mon. Wea. Rev.*, **130**, 2649–2670, doi:10.1175/1520-0493(2002)130<2649:TJMTSP>2.0.CO;2.

——, and L. J. Wicker, 2009: Additive noise for storm-scale ensemble data assimilation. *J. Atmos. Oceanic Technol.*, **26**, 911–927, doi:10.1175/2008JTECHA1156.1.

Emanuel, K. A., 1994: *Atmospheric Convection*. Oxford University Press, 592 pp.

Finley, C. A., and B. D. Lee, 2008: Mobile mesonet observations of an intense RFD and multiple RFD gust fronts in the May 23 Quinter, Kansas tornadic supercell during TWISTEX 2008. *24th Conf. on Severe Local Storms*, Savannah, GA, Amer. Meteor. Soc., P3.18.

Frame, J., P. Markowski, Y. Richardson, J. Straka, and J. Wurman, 2009: Polarimetric and dual-Doppler radar observations of the Lipscomb County, Texas, supercell thunderstorm on 23 May 2002. *Mon. Wea. Rev.*, **137**, 544–561, doi:10.1175/2008MWR2425.1.

French, M. M., H. B. Bluestein, I. PopStefanija, C. A. Baldi, and R. T. Bluth, 2014: Mobile, phased-array, Doppler radar observations of tornadoes at X band. *Mon. Wea. Rev.*, **142**, 1010–1036, doi:10.1175/MWR-D-13-00101.1.

——, D. W. Burgess, E. R. Mansell, and L. J. Wicker, 2015: Bulk hook echo raindrop sizes retrieved using mobile, polarimetric Doppler radar observations. *J. Appl. Meteor. Climatol.*, **54**, 423–450, doi:10.1175/JAMC-D-14-0171.1.

Fujita, T. T., 1975: New evidence from April 3-4, 1974 tornadoes. Preprints, *Ninth Conf. on Severe Local Storms*, Norman, OK, Amer. Meteor. Soc., 248–255.

Grzych, M. L., B. D. Lee, and C. A. Finley, 2007: Thermodynamic analysis of supercell rear-flank downdrafts from Project ANSWERS. *Mon. Wea. Rev.*, **135**, 240–246, doi:10.1175/MWR3288.1.

Hane, C. E., and P. S. Ray, 1985: Pressure and buoyancy fields derived from Doppler radar data in a tornadic thunderstorm. *J. Atmos. Sci.*, **42**, 18–35, doi:10.1175/1520-0469(1985)042<0018:PABFDF>2.0.CO;2.

Hirth, B. D., J. L. Schroeder, and C. C. Weiss, 2008: Surface analysis of the rear-flank downdraft outflow in two tornadic supercells. *Mon. Wea. Rev.*, **136**, 2344–2363, doi:10.1175/2007MWR2285.1.

Klemp, J. B., and R. Rotunno, 1983: A study of the tornadic region within a supercell thunderstorm. *J. Atmos. Sci.*, **40**, 359–377, doi:10.1175/1520-0469(1983)040<0359:ASOTTR>2.0.CO;2.

Kosiba, K., J. Wurman, Y. Richardson, P. Markowski, P. Robinson, and J. Marquis, 2013: Genesis of the Goshen County, Wyoming, tornado on 5 June 2009 during VORTEX2. *Mon. Wea. Rev.*, **141**, 1157–1181, doi:10.1175/MWR-D-12-00056.1.

Lee, B. D., C. A. Finley, and P. Skinner, 2004a: Thermodynamic and kinematic analysis of multiple RFD surges for the 24 June 2003 Manchester, SD cyclic tornadic supercell during Project ANSWERS 2003. *22nd Conf. on Severe Local Storms*, Hyannis, MA, Amer. Meteor. Soc., P11.2.

——, ——, and ——, 2004b: High resolution mobile mesonet observations of RFD surges in the June 9 Basset, Nebraska supercell during Project ANSWERS 2003. *22nd Conf. on Severe Local Storms*, Hyannis, MA, Amer. Meteor. Soc., P11.3.

——, ——, and T. M. Samaras, 2008: Thermodynamic and kinematic analysis near and within the Tipton, KS tornado on May 29 during TWISTEX 2008. *24th Conf. on Severe Local Storms*, Savannah, GA, Amer. Meteor. Soc., P3.13.

——, ——, and C. D. Karstens, 2012: The Bowdle, South Dakota, cyclic tornadic supercell of 22 May 2010: Surface analysis of rear-flank downdraft evolution and multiple internal surges. *Mon. Wea. Rev.*, **140**, 3419–3441, doi:10.1175/MWR-D-11-00351.1.

Lemon, L. R., and C. A. Doswell, 1979: Severe thunderstorm evolution and mesocyclone structure as related to tornadogenesis. *Mon. Wea. Rev.*, **107**, 1184–1197, doi:10.1175/1520-0493(1979)107<1184:STEAMS>2.0.CO;2.

Lewellen, D. C., W. S. Lewellen, and J. Xia, 2000: The influence of a local swirl ratio on tornado intensification near the surface. *J. Atmos. Sci.*, **57**, 527–544, doi:10.1175/1520-0469(2000)057<0527:TIOALS>2.0.CO;2.

Markowski, P. M., J. M. Straka, and E. N. Rasmussen, 2002: Direct surface thermodynamic observations within the rear-flank downdrafts of nontornadic and tornadic supercells. *Mon. Wea. Rev.*, **130**, 1692–1721, doi:10.1175/1520-0493(2002)130<1692:DSTOWT>2.0.CO;2.

——, ——, and ——, 2003: Tornadogenesis resulting from the transport of circulation by a downdraft: Idealized numerical simulations. *J. Atmos. Sci.*, **60**, 795–823, doi:10.1175/1520-0469(2003)060<0795:TRFTTO>2.0.CO;2.

——, M. Majcen, Y. Richardson, J. Marquis, and J. Wurman, 2011: Characteristics of the wind field in three nontornadic low-level mesocyclones observed by the Doppler on Wheels radars. *Electron. J. Severe Storms Meteor.*, **6** (3). [Available online at http://www.ejssm.org/ojs/index.php/ejssm/article/viewArticle/75.]

——, and Coauthors, 2012a: The pretornadic phase of the Goshen County, Wyoming, supercell of 5 June 2009 intercepted by VORTEX2. Part I: Evolution of kinematic and surface thermodynamic fields. *Mon. Wea. Rev.*, **140**, 2887–2915, doi:10.1175/MWR-D-11-00336.1.

——, Y. Richardson, J. Marquis, J. Wurman, K. Kosiba, P. Robinson, E. Rasmussen, and D. Dowell, 2012b: The pretornadic phase of the Goshen County, Wyoming, supercell of 5 June 2009 intercepted by VORTEX2. Part II: Intensification of low-level rotation. *Mon. Wea. Rev.*, **140**, 2916–2938, doi:10.1175/MWR-D-11-00337.1.

Marquis, J. N., Y. P. Richardson, J. M. Wurman, and P. M. Markowski, 2008: Single- and dual-Doppler analysis of a tornadic vortex and surrounding storm scale flow in the Crowell, TX, supercell of 30 April 2000. *Mon. Wea. Rev.*, **136**, 5017–5043, doi:10.1175/2008MWR2442.1.

——, ——, P. M. Markowski, D. Dowell, and J. Wurman, 2012: Tornado maintenance investigated with high-resolution dual-Doppler and EnKF analysis. *Mon. Wea. Rev.*, **140**, 3–27, doi:10.1175/MWR-D-11-00025.1.

——, ——, ——, ——, ——, K. Kosiba, P. Robinson, and G. Romine, 2014a: An investigation of the Goshen County, Wyoming, tornadic supercell of 5 June 2009 using EnKF assimilation of mobile mesonet and radar observations collected during VORTEX2. Part I: Experiment design and verification of the EnKF analyses. *Mon. Wea. Rev.*, **142**, 530–554, doi:10.1175/MWR-D-13-00007.1.

——, P. M. Markowski, Y. P. Richardson, J. Wurman, and K. Kosiba, 2014b: Evolution of angular momentum within observed tornadic mesocyclones. *27th Conf. on Severe Local Storms*, Madison, WI, Amer. Meteor. Soc., 9.5.

Mashiko, W., H. Niino, and T. Kato, 2009: Numerical simulation of tornadogenesis in an outer-rainband minisupercell of Typhoon Shanshan on 17 September 2006. *Mon. Wea. Rev.*, **137**, 4238–4260, doi:10.1175/2009MWR2959.1.

Noda, A. T., and H. Niino, 2010: A numerical investigation of a supercell tornado: Genesis and vorticity budget. *J. Meteor. Soc. Japan*, **88**, 135–159, doi:10.2151/jmsj.2010-203.

Potvin, C. K., and L. J. Wicker, 2013: Correcting fast-mode pressure errors in storm-scale ensemble Kalman filter analyses. *Adv. Meteor.*, **2013**, 624931, doi:10.1155/2013/624931.

Rasmussen, E. N., and J. M. Straka, 2007: Evolution of low-level angular momentum in the 2 June 1995 Dimmitt, Texas, tornado cyclone. *J. Atmos. Sci.*, **64**, 1365–1378, doi:10.1175/JAS3829.1.

Richardson, Y., P. M. Markowski, J. Marquis, J. Wurman, K. Kosiba, P. Robinson, D. Burgess, and C. Weiss, 2012: Tornado maintenance and demise in the Goshen County, Wyoming supercell of 5 June 2009 intercepted by VORTEX2. *26th Conf. on Severe Local Storms*, Nashville, TN, Amer. Meteor. Soc., 13.3. [Available online at https://ams.confex.com/ams/26SLS/webprogram/Paper212526.html.]

Rotunno, R., and J. B. Klemp, 1985: On the rotation and propagation of simulated supercell thunderstorms. *J. Atmos. Sci.*, **42**, 271–292, doi:10.1175/1520-0469(1985)042<0271:OTRAPO>2.0.CO;2.

Schenkman, A. D., M. Xue, and M. Hu, 2014: Tornadogenesis in a high-resolution simulation of the 8 May 2003 Oklahoma City supercell. *J. Atmos. Sci.*, **71**, 130–154, doi:10.1175/JAS-D-13-073.1.

——, ——, and D. T. Dawson, 2016: The cause of internal outflow surges in a high-resolution simulation of the 8 May 2003 Oklahoma City tornadic supercell. *J. Atmos. Sci.*, **73**, 353–370, doi:10.1175/JAS-D-15-0112.1.

Skinner, P. S., C. C. Weiss, M. M. French, H. B. Bluestein, P. M. Markowski, and Y. P. Richardson, 2014: VORTEX2 Observations of a low-level mesocyclone with multiple internal rear-flank downdraft momentum surges in the 18 May 2010 Dumas, Texas, supercell. *Mon. Wea. Rev.*, **142**, 2935–2960, doi:10.1175/MWR-D-13-00240.1.

——, ——, L. J. Wicker, C. K. Potvin, and D. C. Dowell, 2015: Forcing mechanisms for an internal rear-flank downdraft momentum surge in the 18 May 2010 Dumas, Texas, supercell. *Mon. Wea. Rev.*, **143**, 4305–4330, doi:10.1175/MWR-D-15-0164.1.

Supinie, T. A., Y. Jung, M. Xue, D. J. Stensrud, M. M. French, and H. B. Bluestein, 2016: Impact of VORTEX2 observations on analyses and forecasts of the 5 June 2009 Goshen County, Wyoming, supercell. *Mon. Wea. Rev.*, **144**, 429–449, doi:10.1175/MWR-D-15-0171.1.

Wakimoto, R. M., C. Liu, and H. Cai, 1998: The Garden City, Kansas, storm during VORTEX95. Part I: Overview of the storm's life cycle and mesocyclogenesis. *Mon. Wea. Rev.*, **126**, 372–392, doi:10.1175/1520-0493(1998)126<0372:TGCKSD>2.0.CO;2.

——, N. Atkins, and J. Wurman, 2011: The LaGrange tornado during VORTEX2. Part I: Photogrammetric analysis of the tornado combined with single-Doppler radar data. *Mon. Wea. Rev.*, **139**, 2233–2258, doi:10.1175/2010MWR3568.1.

——, P. Stauffer, W.-C. Lee, N. T. Atkins, and J. Wurman, 2012: Finescale structure of the LaGrange, Wyoming, tornado during VORTEX2: GBVTD and photogrammetric analyses. *Mon. Wea. Rev.*, **140**, 3397–3418, doi:10.1175/MWR-D-12-00036.1.

Weiss, C. C., D. C. Dowell, J. L. Schroeder, P. S. Skinner, A. E. Reinhart, P. M. Markowski, and Y. P. Richardson, 2015: A comparison of near-surface buoyancy and baroclinicity across three VORTEX2 supercell intercepts. *Mon. Wea. Rev.*, **143**, 2736–2753, doi:10.1175/MWR-D-14-00307.1.

Wicker, L. J., and R. B. Wilhelmson, 1995: Simulation and analysis of tornado development and decay within a three-dimensional supercell thunderstorm. *J. Atmos. Sci.*, **52**, 2675–2703, doi:10.1175/1520-0469(1995)052<2675:SAAOTD>2.0.CO;2.

Wurman, J., Y. Richardson, C. Alexander, S. Weygandt, and P. F. Zhang, 2007: Dual-Doppler and single-Doppler analysis of a tornadic storm undergoing mergers and repeated tornadogenesis. *Mon. Wea. Rev.*, **135**, 736–758, doi:10.1175/MWR3276.1.

——, K. Kosiba, P. Markowski, Y. Richardson, D. Dowell, and P. Robinson, 2010: Finescale single- and dual-Doppler analysis of tornado intensification, maintenance, and dissipation in the Orleans, Nebraska, supercell. *Mon. Wea. Rev.*, **138**, 4439–4455, doi:10.1175/2010MWR3330.1.

——, D. Dowell, Y. Richardson, P. Markowski, E. Rasmussen, D. Burgess, L. Wicker, and H. Bluestein, 2012: The second verification of the origins of rotation in tornadoes experiment: VORTEX2. *Bull. Amer. Meteor. Soc.*, **93**, 1147–1170, doi:10.1175/BAMS-D-11-00010.1.

——, K. Kosiba, and P. Robinson, 2013: In-situ Doppler radar and video observations of the interior structure of a tornado and wind–damage relationship. *Bull. Amer. Meteor. Soc.*, **94**, 835–846, doi:10.1175/BAMS-D-12-00114.1.